



Article

Optical and Microphysical Properties of the Aerosols during a Rare Event of Biomass-Burning Mixed with Polluted Dust

Marilena Gidarakou ^{1,*}, Alexandros Papayannis ^{1,2,*}, Panagiotis Kokkalis ³, Nikolaos Evangelou ⁴, Stergios Vratolis ⁵, Emmanouella Remoundaki ⁶, Christine Groot Zwaftink ⁴, Sabine Eckhardt ⁴, Igor Veselovskii ⁷, Maria Mylonaki ⁸, Athina Argyrouli ^{9,10}, Konstantinos Eleftheriadis ⁵, Stavros Solomos ¹¹ and Maria I. Gini ⁵

- ¹ Laser Remote Sensing Unit (LRSU), Department of Physics, National Technical University of Athens (NTUA), 15780 Zografou, Greece
² Laboratory of Atmospheric Processes and Their Impact (LAPI), École Polytechnique Fédérale de Lausanne (EPFL), 1015 Lausanne, Switzerland
³ Physics Department, Kuwait University, P.O. Box 5669, Safat 1306, Kuwait
⁴ The Climate and Environmental Research Institute NILU, 2007 Kjeller, Norway
⁵ Environmental Radioactivity & Aerosol Technology for Atmospheric & Climate Impact Laboratory, Institute of Nuclear & Radiological Sciences and Technology, Energy & Safety, National Centre of Scientific Research Demokritos, 15310 Athens, Greece
⁶ Laboratory of Environmental Science and Engineering, School of Mining and Metallurgical Engineering, National Technical University of Athens, 15780 Zografou, Greece
⁷ A. M. Prokhorov General Physics Institute of the Russian Academy of Sciences, Vavilov St. 38, 119991 Moscow, Russia
⁸ Meteorological Institute, Ludwig-Maximilians-Universität München, 80539 Munich, Germany
⁹ Remote Sensing Technology, School of Engineering and Design, Technical University of Munich, 80333 Munich, Germany
¹⁰ German Aerospace Center (DLR), Remote Sensing Technology Institute, 82234 Weßling, Germany
¹¹ Research Centre for Atmospheric Physics and Climatology, Academy of Athens, 10679 Athens, Greece
^{*} Correspondence: marilenagidarakou@mail.ntua.gr (M.G.); apdlidar@central.ntua.gr (A.P.)



Citation: Gidarakou, M.; Papayannis, A.; Kokkalis, P.; Evangelou, N.; Vratolis, S.; Remoundaki, E.; Groot Zwaftink, C.; Eckhardt, S.; Veselovskii, I.; Mylonaki, M.; et al. Optical and Microphysical Properties of the Aerosols during a Rare Event of Biomass-Burning Mixed with Polluted Dust. *Atmosphere* **2024**, *15*, 190. <https://doi.org/10.3390/atmos15020190>

Academic Editor: Mao Mao

Received: 13 December 2023

Revised: 24 January 2024

Accepted: 29 January 2024

Published: 1 February 2024



Copyright: © 2024 by the authors. Licensee MDPI, Basel, Switzerland. This article is an open access article distributed under the terms and conditions of the Creative Commons Attribution (CC BY) license (<https://creativecommons.org/licenses/by/4.0/>).

Abstract: A rare event of mixed biomass-burning and polluted dust aerosols was observed over Athens, Greece (37.9° N, 23.6° E), during 21–26 May 2014. This event was studied using a synergy of a 6-wavelength elastic-Raman-depolarization lidar measurements, a CIMEL sun photometer, and in situ instrumentation. The FLEXPART dispersion model was used to identify the aerosol sources and quantify the contribution of dust and black carbon particles to the mass concentration. The identified air masses were found to originate from Kazakhstan and Saharan deserts, under a rare atmospheric pressure system. The lidar ratio (LR) values retrieved from the Raman lidar ranged within 25–89 sr (355 nm) and 35–70 sr (532 nm). The particle linear depolarization ratio (δ_{aer}) ranged from 7 to 28% (532 nm), indicating mixing of dust with biomass-burning particles. The aerosol optical depth (AOD) values derived from the lidar ranged from 0.09–0.43 (355 nm) to 0.07–0.25 (532 nm). An inversion algorithm was used to derive the mean aerosol microphysical properties (mean effective radius (r_{eff})), single scattering albedo (SSA), and mean complex refractive index (m)) inside selected atmospheric layers. We found that r_{eff} was $0.12\text{--}0.51$ (± 0.04) μm , SSA was $0.94\text{--}0.98$ (± 0.19) (at 532 nm), while m ranged between 1.39 (± 0.05) + 0.002 (± 0.001) i and 1.63 (± 0.05) + 0.008 (± 0.004) i . The polarization lidar photometer networking (POLIPHON) algorithm was used to estimate the vertical profile of the mass concentration for the dust and non-dust components. A mean mass concentration of $15 \pm 5 \mu\text{g m}^{-3}$ and $80 \pm 29 \mu\text{g m}^{-3}$ for smoke and dust was estimated for selected days, respectively. Finally, the retrieved aerosol microphysical properties were compared with column-integrated sun photometer CIMEL data with good agreement.

Keywords: Raman lidar; aerosols; dust; biomass-burning; Sahara; Kazakhstan; FLEXPART; MODIS; optical properties; microphysical properties; CIMEL sun photometer; aerosol mass concentration

1. Introduction

Aerosols play a crucial role in the Earth's radiation budget in a direct way, through scattering and absorption of the solar and terrestrial radiation, as well as by acting as cloud condensation nuclei (CCN), influencing clouds' optical and microphysical properties (indirect way) [1,2]. Arid and semi-arid areas are contributing the most in terms of natural aerosol repositories. In the northern hemisphere, major dust source regions are located in the so-called dust belt spanning from the Saharan desert in Africa to the Taklimakan and Gobi deserts in central and East Asia [3]. Mineral dust is a significant component, representing approximately 75% of the global aerosol mass load and 25% of the global aerosol optical depth (AOD) [4]. Dust originating from different sources exhibits variations in mineralogical composition [5]; optical properties [6–9]; and, consequently, different effects on solar/Earth radiation and climate [10–13]. Typical sources of biomass-burning (BB) aerosols are forest fires (natural and anthropogenic) and agricultural and grassland burnings. BB is responsible for a larger fraction of global mean emissions of black carbon (BC) and organic carbon (OC) [14]. Additionally, BB is a significant source of carbonaceous aerosols [15]. The optical properties of smoke depend on the geographical source region, the season, and the type of BB aerosol [16,17]. Aerosols from BB sources can induce either warming or cooling effects on the climate [18,19].

Although several studies have been carried out regarding the long-range transport of polluted desert dust, mainly from the Sahara, mixed with biomass-burning aerosol from local or regional emissions [20–24], there are still limited cases observed of dust transport from both the Sahara and other desert regions (e.g., Syria, Aralkum, South Kazakhstan) at the same time [9,25–27]. These studies have mainly focused on vertical profiling of the aerosol optical and microphysical properties retrieved by multi-wavelength Raman lidars and sun-photometer data.

Motivated by these observational gaps and to further obtain representative data regarding the profiling of the aerosol optical and microphysical properties of mixed dust and biomass-burning particles, we employed a synergy of instrumentation (Raman and depolarization lidar, sun-photometer, PM Quartz filter samples, OC-EC Aerosol Analyzer) in order to obtain accurate aerosol vertical profiles of optical (backscattering and extinction coefficients, lidar ratio-LR, Ångström exponent) and microphysical (effective radius, single-scattering albedo, and complex refractive index) properties, as well as the chemical composition of dust and biomass-burning aerosols at ground level. Our data could be used to further improve our understanding of the aerosol radiative forcing mechanisms and to reduce the relevant associated uncertainties of climate-forecasting models [28–33].

Here, we present a rare case of a simultaneous transport of dust (from Kazakhstan and Saharan deserts) and biomass-burning aerosols (from South Russia), observed using remote sensing instrumentation (multi-wavelength Raman-depolarization lidar, CIMEL sun photometer), in situ aerosol sampling, and modeling (microphysical inversion schemes and FLEXPART model) to retrieve a complete set of the aerosols' optical, microphysical, and chemical properties. This 6-day long-range transport event was observed over Athens, Greece, on 21–26 May 2014. At first, we present the instrumentation and methodology used for retrieving the aerosol properties, as well as the dust and BB particle dispersion model to justify their origin (Section 2). Our analysis regarding the properties of mixed aerosols (dust and biomass-burning), as derived from the synergy of remote sensing and in situ techniques, is presented in Section 3, with emphasis on the days with optimal lidar retrievals. Finally, in Section 4, we present our final remarks and conclusions.

2. Methodology and Instrumentation

2.1. Raman and Depolarization Lidar Systems for the Retrieval of the Aerosol Optical Properties

At the National Technical University of Athens (NTUA) a compact, 6-wavelength Raman lidar system (EOLE) was used to perform vertical profile measurements of the aerosol optical properties in the Planetary Boundary Layer (PBL) and the lower troposphere. The lidar system is based on a pulsed Nd:YAG laser emitting simultaneously at

355, 532, and 1064 nm with energies of 240, 310, and 260 mJ, respectively, at a repetition rate of 10 Hz. The elastically backscattered lidar signals (at 355, 532 and 1064 nm), as well as those produced by Raman scattering by the atmospheric N₂ (at 387 and 607 nm) and H₂O (at 407 nm), were simultaneously recorded by photomultipliers (PMTs) and avalanche photodiode systems (APD) after spectral separation of the returned lidar signals. The lidar signals detected at 355, 387, 532, 607, and 1064 nm were used to derive the aerosol backscatter (at 355, 532 and 1064 nm), the extinction (at 355 and 532 nm) coefficient, and the Ångström exponent (AE) profiles [33], while the 407 nm channel was used to derive the water vapor mixing ratio profile [34].

To achieve reliable and quantitative lidar aerosol retrievals, a combination of various techniques and methods is necessary. The elastic backscatter lidar technique proves suitable for retrieving aerosol parameters, particularly for moderate aerosol optical depths (AOD < 0.2–0.3 in the visible), assuming a reference height in an aerosol-free area, such as the upper troposphere. In these conditions, the Klett inversion technique [35] is employed to extract the vertical profile of the aerosol backscatter coefficient (b_{aer}) at the respective wavelengths (355, 532, and 1064 nm) during daytime, assuming a constant lidar ratio profile. The resulting average uncertainty of the retrieved b_{aer} values (incorporating both statistical and systematic errors over a 30–60 min averaging time) in the troposphere is of the order of 20–30% [36]. To address this substantial uncertainty, the Raman N₂ lidar technique is applied during nighttime, when the atmospheric background is low, given the relatively weak nature of Raman signals.

In the case of the Raman technique, the measurements of the elastic (355 and 532 nm) and the N₂ Raman backscatter signals (387 and 607 nm) allow for the retrieval of the vertical profiles of the aerosol extinction (a_{aer}) and backscatter coefficients independently of each other [37–39], and, thus, of the lidar ratio ($LR = a_{aer}/b_{aer}$) at 355 and 532 nm. The uncertainties associated with the retrieved b_{aer} and a_{aer} vertical profiles are of the order of 10–20% and 10–15%, respectively [39,40]. Therefore, the corresponding LR uncertainties range from 14 to 25%, while for the AE related to backscatter (AE_b) and extinction (AE_e), they range from 20 to 35% and 20 to 30%, respectively.

Additionally, the mobile elastic depolarization lidar system AIAS of NTUA was used to provide the vertical δ_{aer} in the troposphere, and to evaluate the sphericity of the examined aerosols [41,42]. AIAS operates on a pulsed Nd:YAG laser, emitting at 532 nm, with an energy of 98 mJ pulse⁻¹ at a 10 Hz repetition frequency. The laser beam achieves a vertical polarization of (>99%) through a zero-order $\lambda/2$ waveplate. Subsequently, it is expanded using a Galilean telescope ($\times 4$) before being emitted into the atmosphere, exhibiting a divergence of less than 0.5 mrad. A 200 mm Dall-Kirkham Cassegrainian telescope (focal length $f = 1000$ mm) collects the elastically backscattered light at 2 polarization planes: parallel and perpendicular, with respect to the emitted polarization plane. A secondary mirror directs the collected light to the collimating lenses, dichroic beam splitters, polarizing cubes, doublets, and interference filters (IFF) placed in front of the PMTs. The polarizing cube beam splitter, attached to a rotatable base, is employed for the separation of the co-polarized and de-polarized light at 532 nm. AIAS uses the $\pm 45^\circ$ ($\pm 0.2^\circ$ uncertainty) calibration technique, as described in [41,42]. The retrieved δ_{aer} values exhibit a relative uncertainty of the order of 15%.

2.2. The Flexible Particle Air Mass Dispersion Model (FLEXPART)

To identify the aerosol sources of the case studies presented in Section 3, we used the Lagrangian particle dispersion model FLEXPART, version 10.4 [43,44]. The model was driven by ERA5 [45] assimilated meteorological analyses from the European Centre for Medium-Range Weather Forecasts (ECMWF) with 137 vertical layers, a horizontal resolution of 0.5×0.5 , and hourly temporal resolution. FLEXPART releases computational particles at 0–5000 m heights from the receptor (NTUA) that are tracked backward in time using FLEXPART's "retroplume" mode. Simulations extended over 30 days backward in time, sufficient to include most BC and dust emissions arriving at the station given a typical

aerosol lifetime of 1 week [14]. For each observation and height, the source–receptor matrix (SRM) (also known as “footprint emission sensitivity”, or “footprint”) was calculated; this resulted in a modeled concentration at the receptor when coupled with gridded emissions from an emission inventory. The emission sensitivity expresses the probability of any release occurring in each grid-cell to arrive at the receptor. FLEXPART considers gravitational settling for spherical particles of the observed size, and differs from trajectory models due to its ability to simulate dry and wet deposition of gases or aerosols, turbulence, and unresolved mesoscale motions, while it includes a deep convection scheme [43,44].

The source contributions to the modeled receptor BC were derived by combining each gridded emission sector from the ECLIPSEv6 emission inventory [46] for anthropogenic sources (namely, gas flaring, transportation, shipping, industrial combustion, transportation, domestic combustion, and waste management) and GFEDv4 emission inventory for biomass burning [47] with the footprint emission sensitivity. Dust emissions were computed 3-hourly at 0.25 degrees of spatial resolution using FLEXDUST [48] driven by ECMWF operational analysis fields at 0.25 degrees. Dust particles with diameters up to 17.32 micrometers were included in this study.

2.3. The MODIS Instrument

The Moderate Resolution Imaging Spectroradiometer (MODIS) instruments on board Terra and Aqua satellites [49] provided active fire data throughout the study period. The data distribution occurred through the Fire Information for Resource Management System (FIRMS) (<https://firms.modaps.eosdis.nasa.gov/map>) (accessed on 25 January 2024)). The confidence of the fire data was selected to be above 80% in order to provide a high level of assurance regarding the active fires and to ensure that the air masses arriving to Athens overpassed areas that enriched the layers with biomass-burning aerosols, where fire hot spots were detected [50,51].

2.4. The CIMEL Sun Photometer

Sun photometric observations were performed using a CIMEL sun–sky radiometer, part of the Aerosol Robotic Network (AERONET) Global Network (<http://aeronet.gsfc.nasa.gov> (accessed on 25 January 2023)) [52]. The instrument was located at the Research Center for Atmospheric Physics and Climatology of the Academy of Athens (37.97° N, 23.71° E, 130 m a.s.l.). The CIMEL sky–sun photometer is an automated, ground-based radiometer designed to measure the direct solar irradiance and diffuse sky radiance along almucantar and principal solar planes, covering a field of view of 1.20°. The standard measurement of CIMEL involves obtaining sets of direct sun measurements every 15 min and recording sky diffuse almucantar or principal plane data every 30 min. The specific wavelengths used in this instrument’s channels may vary depending on the version, but it always includes filters at 440, 675, 870, 940, and 1020 nm. The data utilized in this study after cloud screening are level 1.5 (AOD, AE, aerosol size distributions, and aerosol microphysical properties) [52]. The aerosol size distributions obtained through inversion correspond to aerosol radii spanning from 0.01 to 15 μm. The anticipated precision of the inversions is within the range of 15–25% for aerosol radii greater than 0.5 μm and 25–100% for radii less than 0.5 μm [52,53]. The uncertainty in AOD is <±0.01 for wavelengths higher than 440 nm [54], or approximately 10% for a nominal AOD of 0.1. Aerosol size distribution values are retrieved by the sky radiance measurements, and the uncertainty is assumed to be <±5% at all four wavelength channels [55,56].

2.5. In Situ Aerosol Measurements

To retrieve the real-time concentration of the equivalent black carbon (EBC), we used the Aethalometer A33 (Magee Scientific, Berkeley, CA, USA), which is a 7-wavelength dual spot instrument that collects aerosol samples at 5 lt min⁻¹ through short conductive tubing on a filter tape, absorbing at 880 nm. The time resolution of the measurements was 1 min, which was then averaged on an hourly basis. Elemental and organic carbon (EC

and OC, respectively) concentrations were obtained via a Thermo-optical analyzer (Lab OC-EC Aerosol Analyzer model, Sunset Laboratory Inc., Tigard, OR, USA) using PM_{2.5} quartz filter samples, while their total mass was obtained via gravimetric analysis. The time resolution of these measurements was 3 h. The EC measurements' repeatability and reproducibility relative standard deviations were 15 and 20%, respectively [57]. Both instruments were located at Demokritos Station (DEM), a member of the Global Atmospheric Watch (GAW) network; the Aerosol, Clouds, and Trace Gases Research Infrastructure (ACTRIS); and the PANhellenic infrastructure for Atmospheric Composition and climatE chAnge (PANACEA). The DEM monitoring site belongs to the National Centre of Scientific Research, "Demokritos", which is situated 7 km to the north from downtown Athens, in a pine forest (37.995° N, 23.816° E, at 270 m a.s.l.). It is representative of the urban background atmospheric aerosol concentration in the Athens metropolitan area [58].

Furthermore, aerosol samples were also collected at NTUA (School of Mining and Metallurgical Engineering), 14 m a.g.l. The sampling location was fully exposed to the wind and was free of obstacles. Between 21 and 23 May, ten PM₁₀ and PM_{2.5} samples were collected over 3 to 5 h on PTFE membranes following the sampling procedure described in [59,60]. The PM₁₀ and PM_{2.5} concentrations were retrieved using the methodology detailed in [60]. Additionally, the concentrations of Cl⁻, NO₃⁻, PO₄⁻³, SO₄²⁻, Na⁺, NH₄⁺, K⁺, Ca²⁺, and Mg²⁺ were determined using ion chromatography, as described in [60].

2.6. Retrieval of the Profiles of the Microphysical Aerosol Properties

The aerosols' microphysical properties within the dust and/or biomass-burning layers were retrieved using the regularization inversion technique [30,61], using the vertical profiles of a_{aer} (at 355–532 nm) and b_{aer} (at 355, 532 and 1064 nm) obtained from the Raman backscattered lidar signals, as well as the depolarization lidar profiles at 532 nm, as input. The inverted aerosol microphysical properties comprised the effective radius (r_{eff}), the total number (N), the surface area (S) and volume (V), as well as the real (Re[m]) and imaginary (Im[m]) parts of the particle refractive index (m) and the single-scattering albedo (SSA) within the different aerosol layers. In our method, we did not consider the spectral dependence of the m or the chemical composition of the aerosol particles. Therefore, the obtained m values represent the average values considering the size and spectral range (355–1064 nm). The particles were considered as spheres ($\delta_{aer} < 10\%$) and spheroids ($\delta_{aer} > 10\%$). We should also note that for the fine mode, the optical properties of the spheres and spheroids were very similar, and significant differences were found only for the coarse mode. The uncertainty of the Re[m] is of the order of ± 0.05 , while for Im[m], it is of the order of $\pm 50\%$. The corresponding uncertainties of the r_{eff} , V, and S are below 20%, while the uncertainty of N can be up to 50% [61].

2.7. Aerosol Mass Concentration Lidar Retrievals

To estimate the aerosol mass concentration profiles (for dust and non-dust components) [62], we used the polarization lidar photometer networking (POLIPHON) algorithm as detailed in [63]. The method relies on the combined data from depolarization lidar measurements and sun photometry observations. The fundamental concept behind this approach is to utilize depolarization lidar data to distinguish the contributions of dust and non-dust aerosol types in the total aerosol backscatter coefficient profile. The sun-sky photometer provides spectrally resolved, column-integrated particle extinction values (AOD) and allows for the retrieval of fine and coarse mode AODs [56,64], as well as the microphysical aerosol properties, including particle volume (v) and surface-area concentrations for the fine- and coarse-mode fractions. Subsequently, the mass concentrations of the dust components are calculated using their well-established properties, including δ_{aer} , LR, mass density, and v/AOD. These properties are estimated based on the sun photometric observations.

In this study, we used a coarse-mode particle density of $\rho_c = 2.6 \text{ g cm}^{-3}$ (desert and mixed dust) [63,65–69] and a fine-mode particle density of $\rho_f = 1.35 \text{ g cm}^{-3}$ [70–73]. The latter measurements were specifically employed to obtain the intensive aerosol prop-

erties. Consequently, satisfactory results can be obtained even when the lidar and sun photometer measurements are not precisely collocated and simultaneously measured. This is particularly applicable to Sahara dust, given that the v/AOD has been observed to remain relatively stable during specific dust events [63]. The uncertainties associated with the retrieved particle mass concentration primarily include two components [62,74,75]: (i) uncertainties in the retrieved backscattering coefficient and depolarization ratio, mainly influenced by the signal-to-noise ratio of the lidar backscattering signals, and (ii) uncertainties attributed to the input parameters of the POLIPHON method [76]. The uncertainties of the backscatter and extinction coefficient as well as the depolarization ratio at 532 nm arose from the discussions in Section 2.1. A reasonable uncertainty of 20% was assumed for the smoke and dust mass density [63,77]. The conversion factor (v/AOD, volume concentration to AOD ratio), which is also required as input, may vary up to 10% and 20% for dust and smoke, respectively [78]. Taking into consideration all of the above, by applying the law of propagation, we found a comprehensive uncertainty of ~36–40% in the particle mass concentration profiles.

3. Case Study: 21–26 May 2014

In the following sub-sections, we present a 6-day period of mixed aerosols (biomass burning and polluted dust) observed over Athens on 21–26 May 2014 at the 1.3–4.3 km height range above sea level (a.s.l.). The atmospheric structure during this period was characterized by the formation of a low-pressure system over the East Balkans and the Black Sea on 14–17 May 2014. This type of circulation favors the transport of air masses from Kazakhstan towards Greece. This pattern was replaced by a prevailing high-pressure system over the central and eastern Mediterranean during the following days (18–25 May 2014). This system enabled the transport of Saharan dust towards Greece. The combination of the above weather types was responsible for the transport of the biomass and Saharan dust aerosols that were detected over Athens during the measuring period (Figures S1 and S2).

The remote sensing and in situ ground instruments were operating continuously during this period, except for the night of 25 May due to extensive cloud cover conditions over the measuring site.

Figure 1 presents the spatio-temporal evolution of the range-corrected lidar signal (in arbitrary units-AU) obtained using EOLE at 1064 nm from 0.3 to 6.0 km height a.s.l., between 21 May and 26 May 2014. On 21 May, the first day of the studied event, two dispersed free tropospheric aerosol layers were observed within ~2.0–6.0 km over a convective planetary boundary layer (PBL) extending up to ~1.8 km in height (06:10–14:54 UTC), while later, during the night hours (18:44–21:50 UTC), the aerosols were confined inside a quite shallow PBL from the ground up to ~1.7 km (Figure 1, upper left). On 22 May, a convection lifted aerosols up to ~2.2 km height in the PBL (from 06:30 to 11:30 UTC), while aerosol remnants were found at 2.2–2.9 km height (~15:00 UTC) (Figure 1, upper middle). Later the same day (18:27–22:00 UTC), the PBL collapsed, leaving a residual aerosol layer extending from 0.8–1.2 to 3.0 km a.s.l. aloft over the PBL top-height.

On 23 May, a deep convection was again formed over Athens (07:25 and 12:32 UTC), uplifting aerosols up to a height of ~3.0 km, where they were mixed with a residual aerosol layer observed at the same height (1.0–3.0 km) during the previous night hours (Figure 1, upper right). Later on, during nighttime (19:08–21:45 UTC), a strong residual layer, rich in aerosols, was observed over a very shallow PBL (with a top at ~0.5 km height) leaving a residual aerosol layer at ~1.0–1.2 km height. Above that height, several discrete aerosol layers were observed up to ~3.2 km a.s.l.

On the following day, 24 May, the PBL remained shallow up to a height of ~1.1 km, while between 18:56–21:50 UTC, a residual layer rich in aerosols and decoupled from the PBL was formed around 1 km a.s.l. Above that layer, several aerosol layers were observed between 1.0 and 5.0 km a.s.l., mostly descending. On 25 May, a thermal convection led the PBL top-height up to ~1.8 km a.s.l., around 12:00 UTC. During the night hours (18:42–21:16 UTC), the PBL was confined below ~0.4 km a.s.l. Again, as on the previous

day, several descending aerosol layers were observed above the PBL, mainly between 1.8 and 4.2 km (daytime hours), extending up to ~5 km (nighttime hours). Finally, on the last day (26 May), the PBL remained quite shallow (PBL top up to ~1.1 km between 05:51 and 15:08 UTC), above which several aerosol layers were observed up to ~5.0 km height, with a very distinct one descending from ~4.0 km (05:51 UTC) down to ~2.0 km a.s.l. (22:00 UTC).

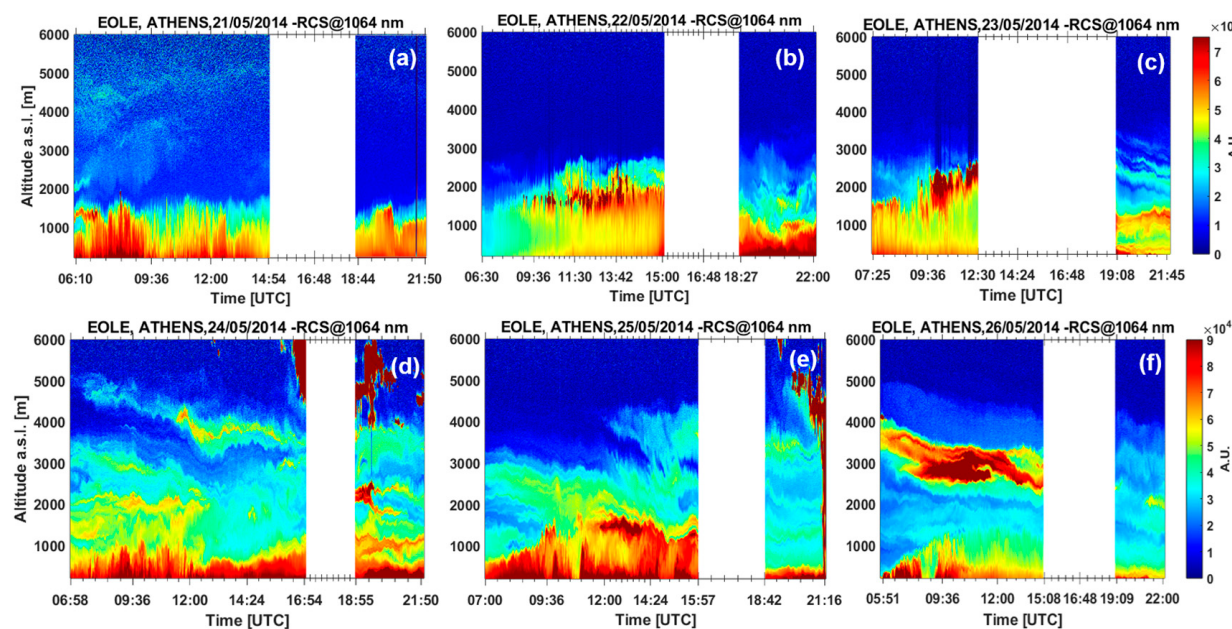


Figure 1. Spatio-temporal evolution of the range-corrected lidar signal obtained by the EOLE lidar at 1064 nm in arbitrary units (A.U.) over Athens (21–26 May 2014) up to 6.0 km height a.s.l.

Figure 2 presents the footprint emission sensitivity for dust, as obtained by FLEXPART for the air masses arriving over Athens between 0.5 and 4.0 km, from 21 to 26 May 2014 (04:00 UTC to 22:00 UTC). The red dots represent active fires retrieved using MODIS (confidence level > 80%), confirming that, in general, the air masses overpassed fire hot spot regions (wildfires/agricultural fires) and the Saharan/Kazakhstan deserts before arriving over the study area.

More specifically, from 21 to 23 May (Figure 2a–c, Figures S3–S6), the “footprint” suggests an increased residence time of air masses along the N.E direction axis (Athens–Black Sea–Caspian Sea–Kazakhstan), including the arid regions around the Aral Sea. The latter is an active salt dust source region due to the desiccation of the lake [79–82]. Therefore, during this period, the air mass trajectory sampled over Athens was enriched with a mixture of desert dust originating from central Kazakhstan and the arid regions around the Aral Sea, and with BB particles emitted from agricultural fires from South Russia and Kazakhstan, as indicated by the FLEXPART and MODIS data.

Regarding the period from 24 to 26 May (Figure 2d–f, Figures S7–S10), the “footprint” suggests that there were two different aerosol source regions potentially affecting the aerosol concentrations over Athens: the Saharan desert, the dominant one, and the agricultural fires and the Kazakhstan area, with much less sensitivity. Therefore, during that period, the air masses arriving over Athens were a mixture of Saharan and Asian dust and biomass-burning aerosols.

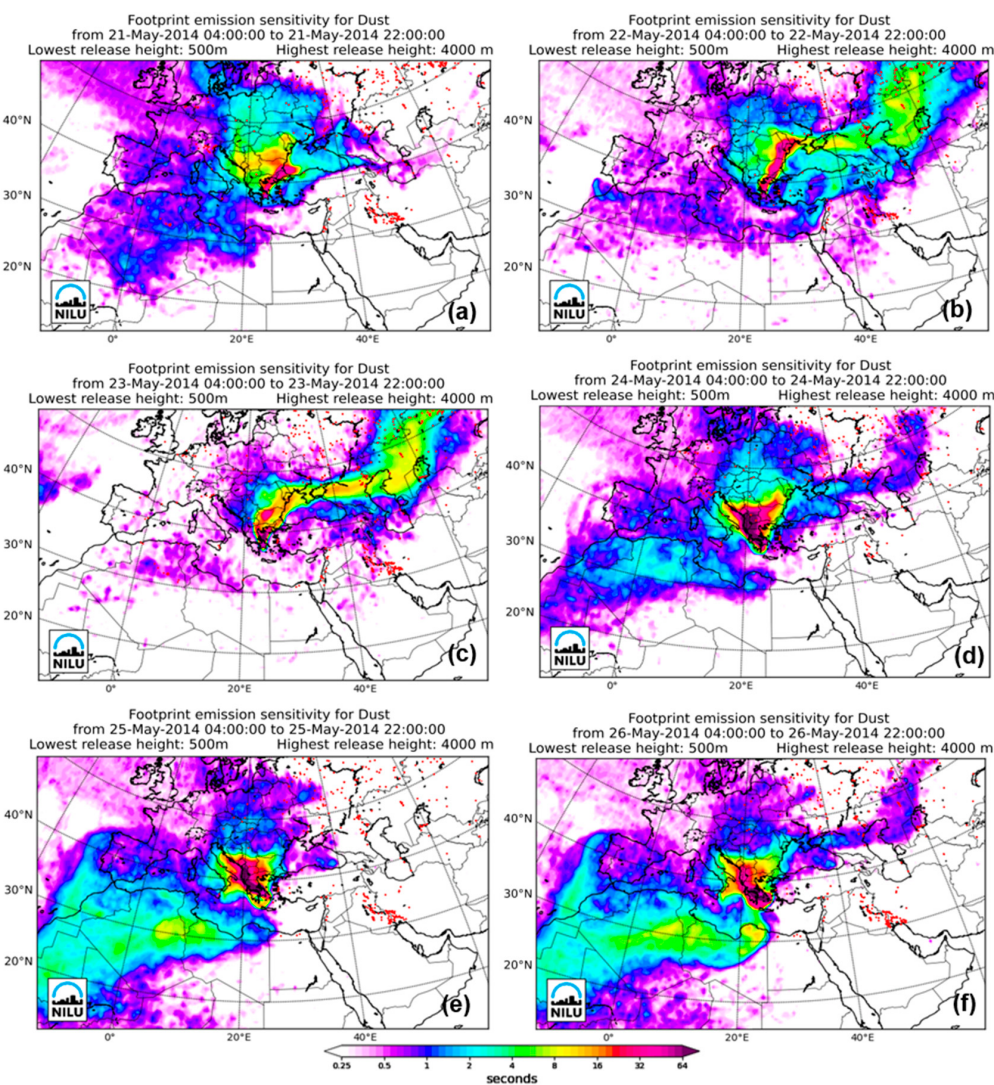


Figure 2. “Footprint” emission sensitivity for dust obtained using FLEXPART for the air masses arriving over Athens between 0.5 and 4.0 km from 21 to 26 May 2014 (04:00 UTC to 22:00 UTC). The red dots represent active fires retrieved by MODIS (confidence level > 80%).

In Figure 3, we present the aerosols’ geometrical and optical properties, obtained using the EOLE and AIAS lidars under cloud-free conditions during the period of 21–26 May 2014. The different color bars denote the tops and the bottoms of the sampled aerosol layers together with the mean values of the $\text{AE}_{\text{b}355/532}$, LR_{355} , δ_{532} , $\text{AE}_{\text{b}532/1064}$, and LR_{532} , as well as their standard deviations.

From the data presented in Figure 3, it can be discerned that the main aerosol layers were found between 1.3 and 4.3 km a.s.l. The retrieved aerosol optical properties showed that the elevated layers (on 21–22 May) were characterized by LRs from 25 to 54 sr (355 nm) (Figure 3c) and 31 to 56 sr (532 nm) (Figure 3f). The δ_{532} values ranged between 5 and 9% (Figure 3d), lower than the typical values [41] usually measured for pure dust. The $\text{AE}_{\text{b}355/532}$ varied from 0.82 to 1.50 (Figure 3b), and the $\text{AE}_{\text{b}532/1064}$ from 0.91 to 1.48 (Figure 3e), which indicated a presence of fine-mode particles.

Particularly on 23 May, high δ_{532} values (19–27%) indicative of the presence of mixed dust particles were observed on that day, which is corroborated by the LR values, which ranged between 33 and 52 sr (355 nm) (Figure 3c) and 41 and 62 sr (532 nm) (Figure 3f). We should also note that the $\text{LR}_{355}/\text{LR}_{532}$ ratio (color ratio) dropped below 1 on that day and ranged between 0.65 to 0.87, which is indicative of fresh biomass-burning air masses [83].

Furthermore, the AE varied from 1 to 2.01, from 1.01 to 1.21 ($\text{AE}_{\text{b}355/532}$) (Figure 3b), and from 0.91 to 1.48 ($\text{AE}_{\text{b}532/1064}$) (Figure 3e). The significantly low values of the color ratio along with the aforementioned AE values are indicative of the presence of mixed biomass-burning and dust aerosols [84–87], which were found to originate from North Kazakhstan and South Russia, as determined via the FLEXPART simulations presented above (Figure 2).

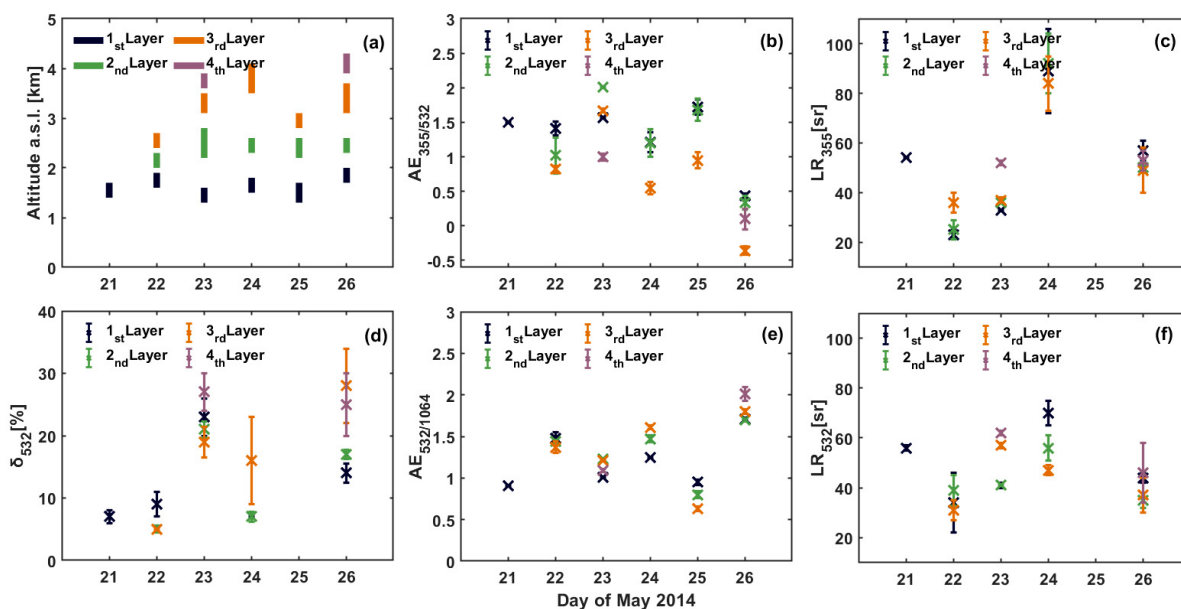


Figure 3. (a) Geometrical and (b–f) mean optical properties of the aerosol layers observed using the EOLE and AIAS lidar systems over Athens, along with their standard deviations (21–26 May 2014).

During the subsequent period (24–26 May), when the air mass trajectories were traced back to the Saharan desert and South Russia, a change in the aerosol optical properties was noted. The LRs increased by almost two times compared to the days before, varying from 84 to 92 sr at 355 nm (Figure 3c) and from 37 to 70 sr at 532 nm (Figure 3c,f), implying the presence of strongly absorbing particles [23]. Concurrently, the δ_{532} exhibited values from 7 to 28% (24–26 May) (Figure 3d) and the AE ranged between −0.36 and 1.68 ($\text{AE}_{\text{b}355/532}$) (Figure 3b) and 0.63 and 2.01 ($\text{AE}_{\text{b}532/1064}$) (Figure 3e). Furthermore, the $\text{LR}_{355}/\text{LR}_{532}$ for these days increased above 1 (1.3–1.8), indicating the presence of aged biomass-burning particles. Specifically, on 26 May, the color ratio values were accompanied by significantly low $\text{AE}_{\text{b}355/532}$ values, which ranged between −0.36 to 0.44, revealing the domination of large dust particles [83,86,88]. These observations corroborate the presence of both polluted dust and smoke aerosols [23,24], as the air mass trajectories originated from the Saharan desert and South Russia.

In Figure 4, we present the temporal variation of the hourly averaged values of OC, EC, and EBC (Figure 4a) accompanied by the daily AOD at visible, with the corresponding contributions from the fine and coarse modes and the AE at 440/870 nm (Figure 4b). The EBC and EC covaried throughout the measurement period ($\text{EBC} \sim 0.13\text{--}1.0 \mu\text{g m}^{-3}$, $\text{EC} \sim 0.14\text{--}1.48 \mu\text{g m}^{-3}$). Notably, during the period of 21–23 May, the mass concentrations of EBC ranged between 0.13 and $0.77 \mu\text{g m}^{-3}$, and those of EC varied from 0.14 to $0.82 \mu\text{g m}^{-3}$. For the following days (24–26 May), slightly elevated mass concentrations were observed for both EBC and EC, spanning $0.30\text{--}1.0 \mu\text{g m}^{-3}$ and $0.30\text{--}1.48 \mu\text{g m}^{-3}$, respectively. Regarding the OC concentrations, a similar pattern was observed for both periods, but with consistently higher mass concentrations ($\text{OC} \sim 0.81\text{--}4.44 \mu\text{g m}^{-3}$) compared to the EBC and EC. Specifically, we found that OC varied between 0.81 and $2.46 \mu\text{g m}^{-3}$ for the period of 21–23 May, and during 24–26 May, an increase in mass concentrations was noted, ranging from 1.34 to $4.4 \mu\text{g m}^{-3}$.

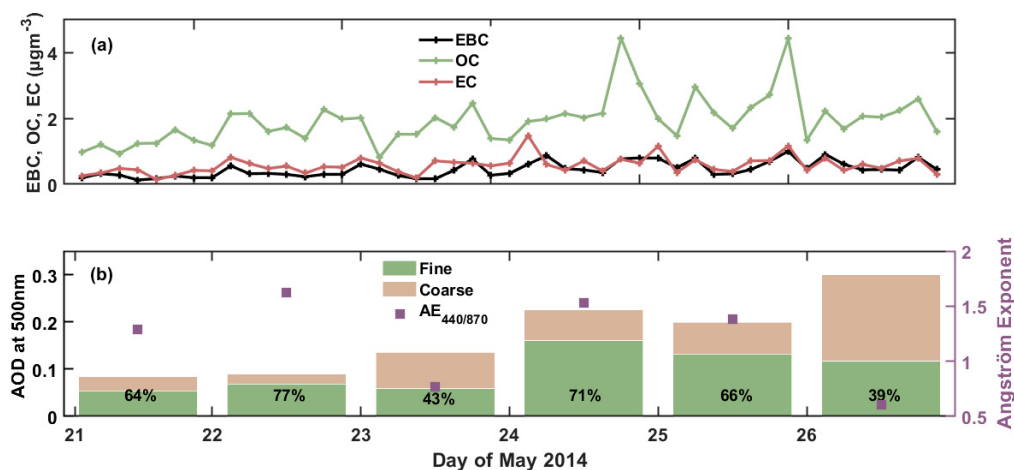


Figure 4. (a) Time—series of hourly averaged values of equivalent black carbon (EBC) (black line), organic carbon (OC) (green line), and elemental carbon (EC) (red line) concentrations measured at ground level (in $\mu\text{g m}^{-3}$); (b) CIMEL fine/coarse-mode aerosol optical depth (AOD); and AE at 440/870 nm (purple squares), obtained over Athens at 500 nm between 21 and 26 May 2014. The percentages show the ratio between the fine and coarse AOD.

The differences in mass concentrations observed during these two periods are due to variations in the sources and the trajectories of the air masses prior to their arrival over Athens. As discussed already in Figure 2, FLEXPART “footprint” analysis outlined that, during the first period (21–23 May) the air masses originating from the Kazakhstan area traversed extensive distances, thus resulting in relatively diminished pollutant concentrations upon reaching Athens. In contrast, during the second period (24–26 May), FLEXPART revealed the diverse origin of the air masses, emanating from the Saharan desert, South Russia, and North Kazakhstan. However, the predominance of air masses originating from the Saharan desert may have potentially led to a lower pollutant dispersion and higher mass concentrations. It should be noted that the PBL was significantly shallower in the second period in comparison to the first period (Figure 1). The higher EBC, OC, and EC concentration values observed during the second period could be partly attributed to this fact.

On 23 May, the concentration of $\text{PM}_{2.5}$ reached the maximum 24 h threshold of $25 \mu\text{g m}^{-3}$ at 14 m above ground level (Figures S12 and S13), indicating that, at ground level, the concentration of $\text{PM}_{2.5}$ was even higher. This was due to the addition of the influx of fine particles transported from North Kazakhstan and South Russia in the local aerosol. Furthermore, the PM_{10} concentration also reached a high value ($42 \mu\text{g m}^{-3}$) due to the presence of coarse particles transported from Kazakhstan Desert [89,90]. Between 21 and 23 May, the observed high concentrations of NO_3^- ($317\text{--}1368 \text{ ng m}^{-3}$ at $\text{PM}_{2.5}$), NH_4^+ ($829\text{--}1311 \text{ ng m}^{-3}$ at $\text{PM}_{2.5}$, $1111\text{--}1663 \text{ ng m}^{-3}$ at PM_{10}), and SO_4^{2-} ($3233\text{--}5488 \text{ ng m}^{-3}$ at $\text{PM}_{2.5}$, $3798\text{--}4204 \text{ ng m}^{-3}$ at PM_{10}) (Figure S14) reflected the presence of biomass-burning aerosols near the ground. More specifically, the NH_4^+ concentrations reflected the presence of biomass-burning and marine aerosols mixed with aerosols originating from the Black Sea [91,92]. Moreover, the concentration of SO_4^{2-} depends upon local and long-range transport of anthropogenically polluted air masses [93,94].

On the other hand, Ca^{2+} and Mg^{2+} ions are present in significant amounts in mineral dust particles [95]. During the study period, a sharp increase in the concentrations of Ca^{2+} ($103\text{--}502 \text{ ng m}^{-3}$ at $\text{PM}_{2.5}$, $370\text{--}1484 \text{ ng m}^{-3}$ at PM_{10}) and Mg^{2+} ($14\text{--}139 \text{ ng m}^{-3}$ at $\text{PM}_{2.5}$, $33\text{--}417 \text{ ng m}^{-3}$ at PM_{10}) was observed in both fine and coarse aerosol samples. The increase was more pronounced for PM_{10} , marking the presence of coarse particles due to dust transportation over Athens. K^+ is an element with a mixed origin in the aerosol: it is contained in the aerosol originating from biomass burning, but it is also contained in dust particles [96–99]. K^+ concentration levels were also elevated in both $\text{PM}_{2.5}$ and PM_{10} samples ($53\text{--}114 \text{ ng m}^{-3}$ at $\text{PM}_{2.5}$, $48\text{--}150 \text{ ng m}^{-3}$ at PM_{10}).

Moreover, in Figure 4b, the AOD values at 500 nm show strong variability. The maximum values of the AOD (~0.3) were found on 26 May, which is indicative of the presence of aerosols reducing the air quality over the Athens Basin [100]. The coarse mode contribution to the total AOD reached its maximum value on 23 (57%) and 26 (61%) May due to presence of mixed Asian and Saharan polluted dust [101], respectively, over Athens, with a corresponding decrease in the AE on these days (daily mean values of 0.76 and 0.61, respectively). The fine-mode particles within the atmospheric column accounted for 64–77% on the remaining days, indicating the dominance of smaller particles, while the mean AE increased up to about 1.45.

Additionally, in Figure 5a, we present the corresponding columnar mean size distribution retrieved by sun photometric measurements over Athens for the period of 21–26 May 2014. The bi-modal size distribution shows particles with radii ranging from 0.14 to 0.19 μm and around 1.8 μm . Specifically, on 21–22 May, the fine particles dominated due to the presence of smoke, while on 23–26 May, the coarse mode became more dominant due to the mixing of smoke and desert dust aerosols. On both 23 May and 26 May, the columnar mean size distribution revealed a predominance of larger particles (with effective radii centered around 1.7 μm) in comparison to smaller ones (with effective radii centered around 0.15 μm). When we compare the experimental size distributions obtained using 24 h cascade impactor aerosol surface measurements at the same location under similar conditions (Figure S17), as discussed in [102], we can observe that the same bi-modal behavior is confirmed at the surface observations in this size range, with a 3rd minor peak appearing above 10 μm . In terms of aerodynamic diameter, the submicron modes in all cases were smaller (0.27–0.3 μm) in the retrieved size distribution compared to the observed size distributions at the surface (0.4 and 0.37 μm for Sahara and background cases, respectively [102]). This can be explained by the difference in aerodynamic and optical diameters used in the two descriptions. This difference was not observed in the coarse mode, where, in all cases, the peak was located between 3.4 and 3.8 μm . This may have been caused by the stronger variability in the coarse particle density between the surface and elevated layers and could be a sensitivity parameter to be tested when elaborating the retrieval algorithms. The chemical compositions observed for Saharan and background aerosol were very similar to that observed at the same location in previous earlier studies [103]. It is confirmed that the distribution of ions like SO_4 , existing almost exclusively in the $\text{PM}_{2.5}$ fraction (Figure S15, Table S1) or Ca^{2+} in the coarse fraction (Figure S16, Table S2), was the same in the current study.

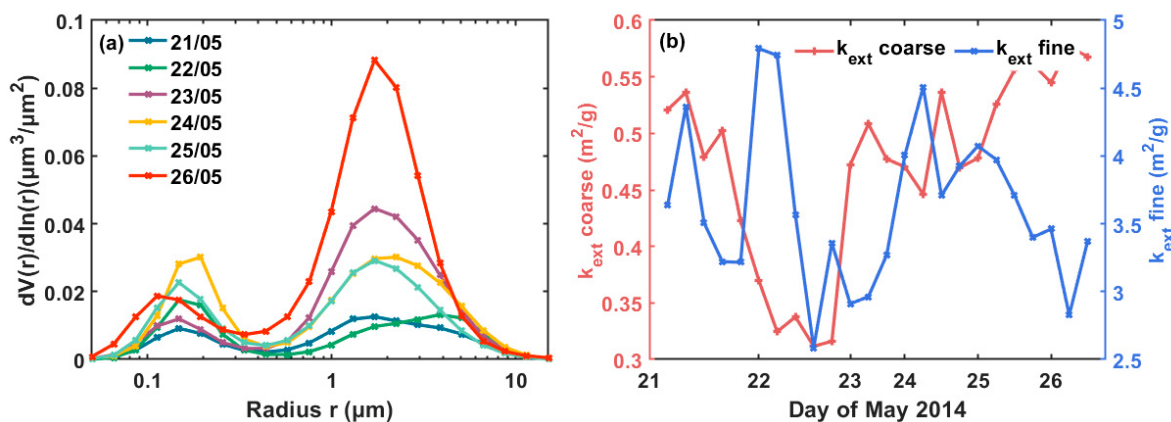


Figure 5. (a) Particle volume size distribution and (b) evolution of the daily mass-specific extinction coefficients (coarse (red line) and fine (blue line) mode) derived from AERONET, NOA CIMEL sun photometer between 21 and 26 May 2014.

The daily mass-specific extinction coefficient (k_{ext}) for the coarse and fine modes, as derived from CIMEL sun photometer during the period of 21–26 May 2014, is presented in Figure 5b. The mass-specific extinction coefficient holds a coarse-mode particle

density of $\rho_c = 2.6 \text{ g cm}^{-3}$ (desert and mixed dust) [63,65–68] and a fine-mode particle density of $\rho_f = 1.35 \text{ g cm}^{-3}$ [70–73]. We observed that the k_{ext} values of the coarse particles ranged between 0.32 and 0.58 $\text{m}^2 \text{ g}^{-1}$. Similar values have been reported for dust particles [63,65,104,105], leading to the conclusion that the k_{ext} values are independent of the distance of the observation from the source [63]. Regarding the fine mode, the k_{ext} values ranged between 2.58 and 4.79 $\text{m}^2 \text{ g}^{-1}$, indicative of the presence of biomass-burning smoke and/or urban haze [65,76,106]. The dispersion of the k_{ext} values for a specific aerosol type can offer insight into the range of uncertainty in the particle mass concentration retrievals when incorporating values from existing literature in the data analysis. The uncertainties related to the retrieval of the k_{ext} values and, therefore, to the particle mass concentration, mainly arise from uncertainties related to the conversion of the backscatter into extinction coefficients caused by the lidar ratio estimation, as well as from the used v/AOD ratio (conversion factor), as discussed in Section 2.7. More details about the errors in the retrieval of mass concentrations can be found in [76].

3.1. Case of 23 May 2014: Aged BB and Dust (Russian Forest Fires and Kazakhstan Dust Aerosols)

The retrieved profiles of b_{aer} (Figure 6a) and δ_{532} (Figure 6b) on 23 May (20:30–21:45 UTC) showed the presence of four elevated layers, characterized by high aerosol backscatter coefficients (Figure S11) and values of δ_{532} ranging from 19–27%, indicating the presence of mixed biomass-burning and dust aerosols [33,62,87,107]. In order to identify the various aerosol layers, we used the gradient method [108] by studying the slope of the backscatter coefficient. The identified layers were found to be: layer 1 (1.32–1.62 km), layer 2 (2.22–2.76 km), layer 3 (3.06–3.48 km), and layer 4 (3.60–3.90 km). Additionally, the inversion algorithm was applied to the mean-layer-derived values of the aerosol optical properties ($3b + 2a + \delta$) to estimate the corresponding mean values of the microphysical properties (r_{eff} , m , SSA).

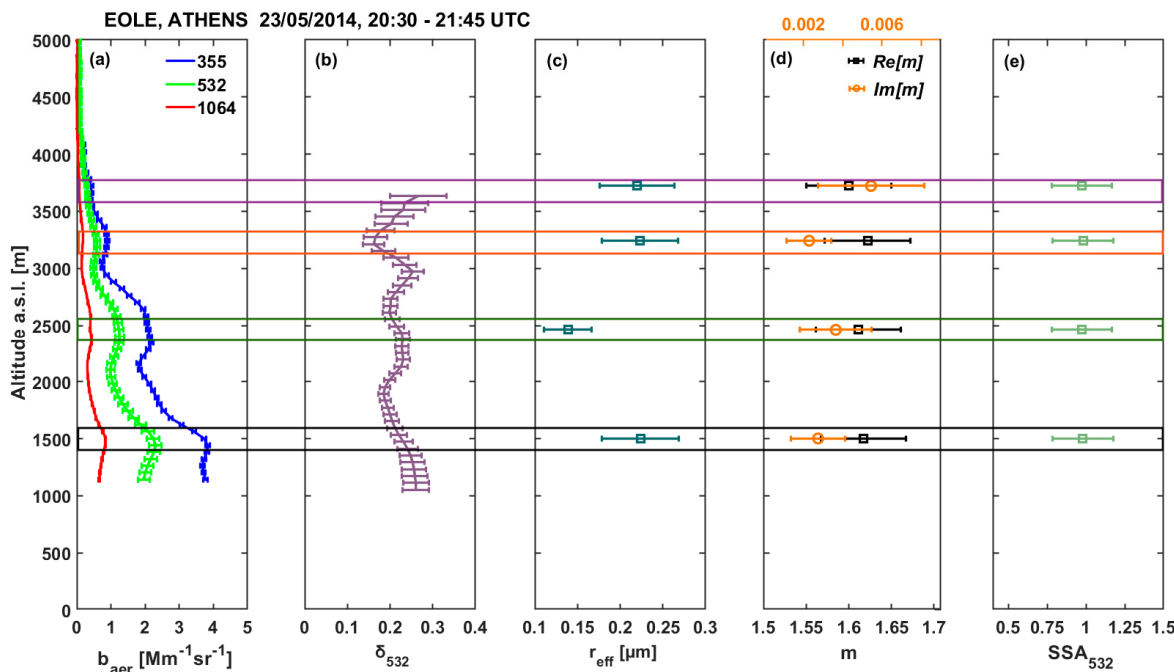


Figure 6. Vertical profiles of the (a) aerosol backscatter at 355 nm (blue line), 532 nm (green line) and 1064 nm (red line) obtained over Athens by the EOLE lidar, (b) particle depolarization ratio (532 nm), (c) the aerosol effective radius, (d) refractive index real part (black line) and imaginary part (orange line), and (e) single-scattering albedo, as estimated by the inversion algorithm using the aerosol optical properties derived from the Raman lidar measurements at 532 nm on 23 May 2014 (20:30–21:45 UTC).

The r_{eff} retrievals (Figure 6c) indicate the vertical homogenous conditions of the mixture of fine and coarse modes at the first, third, and fourth aerosol layers ($r_{\text{eff}} 0.22 \pm 0.04 \mu\text{m}$). However, at the second aerosol layer at 2.46 km, the value of r_{eff} was significantly lower ($r_{\text{eff}} 0.14 \pm 0.03 \mu\text{m}$), but with the highest observed number density of $1363 \pm 333 \text{ cm}^{-3}$ (not shown), showing a significant contribution of fine mode particles due to the mixture of aged, biomass-burning aerosols with dust. Furthermore, a decrease in the number density for the third and fourth layers ($70 \pm 21 \text{ cm}^{-3}$ and $140 \pm 42 \text{ cm}^{-3}$, respectively), indicate the mixing of dust with biomass-burning particles [24].

The real part of the refractive index (Figure 6d) was found to be 1.61 ± 0.05 for all layers, indicating a strong mixing of dust with urban-like sulfate and organic carbon aerosols over Athens [23,109,110]. The imaginary parts of the refractive index were found to be 0.003 ± 0.002 , 0.004 ± 0.002 , and 0.002 ± 0.001 for layers 1, 2, and 3, respectively, while for layer 4, it increased up to 0.005 ± 0.003 , indicating the presence of aerosols mixed with slightly absorbing dust [10,111–114]. The mean SSA values were found to be 0.951 ± 0.195 for all aerosol layers (Figure 6e), confirming the presence of slightly absorbing particles. This is in agreement with a previous observation of Russian fires in Athens in 2010 [115], with elevated SSA values at 532 nm close to 0.91 during the period of the fires. The retrieved microphysical data can be further used as input to the ISORROPIA model to obtain the chemical composition of the aerosols aloft [32,33].

In Figure 7, we present the b_{aer} for the total, fine, and coarse modes, as well as δ_{532} , as derived by the AIAS lidar system, together with a_{aer} and the mass concentration (fine and coarse) on 23 May (14:30–15:30 UTC), using the POLIPHON method discussed in Section 2.7. The vertical profile of total b_{aer} (Figure 7a) indicates moderate backscattering up to 3.5 km. Above a height of 1.5 km, the smoke and dust particles contributed almost equally to the backscattering coefficient. The δ_{532} (Figure 7b) ranging between 16–27% is indicative of a mixture of smoke and dust particles [23,84,86] coming from North Kazakhstan and South Russia, as previously discussed (Figure 2). However, the relevant fine mode (smoke) extinction coefficients (Figure 7c) are rather higher than the coarse (dust) ones, since the smoke lidar ratio was larger than the desert dust one. More specifically, lidar ratios of 75 and 55s were employed to convert backscatter into extinction coefficients, typical for biomass-burning particles (fine mode) and desert dust (coarse mode), respectively [116–120].

Furthermore, to retrieve the aerosol mass concentrations (Figure 7d), we used densities of $\rho_f = 1.35 \text{ g cm}^{-3}$ and $\rho_c = 2.6 \text{ g cm}^{-3}$ for fine (smoke) and coarse (dust) particles [70–73]. Afterwards, we calculated the mean volume concentration to AOD ratio values equal to $v_c/\text{AOD}_c = 0.79 \times 10^{-6} \text{ m}$ (coarse-mode) and $v_f/\text{AOD}_f = 0.21 \times 10^{-6} \text{ m}$ (fine-mode). The mean relevant mass-specific extinction coefficients obtained at the nearest temporal resolution were $k_{\text{ext},c} = 0.50 \text{ m}^2 \text{ g}^{-1}$ and $k_{\text{ext},f} = 3.05 \text{ m}^2 \text{ g}^{-1}$ for coarse-mode and fine-mode particles, respectively, for that day. Thus, a mean smoke mass concentration of $10 \mu\text{g m}^{-3}$ was estimated, while for dust, the mass concentration ranged between 10 ± 4 and $160 \pm 58 \mu\text{g m}^{-3}$ (for a mean AOD_{532} of 0.17). Below a height of 1.5 km, the mean value of smoke mass concentration was found to be approximately equal to $16 \pm 6 \mu\text{g m}^{-3}$, very close to the $\text{PM}_{2.5}$ values ($24.5 \mu\text{g m}^{-3}$) measured at ground level, which were slightly higher than the World Health Organization (WHO) air quality levels (24 h average less than $15 \mu\text{g m}^{-3}$).

On the other hand, the lower-atmospheric mean dust mass concentration values, found to be about $150 \pm 54 \mu\text{g m}^{-3}$ (around 1.5 km height), were almost three times higher than the PM_{10} ($42 \mu\text{g m}^{-3}$) mean concentration at the surface, despite all the different sources of uncertainty for such a comparison.

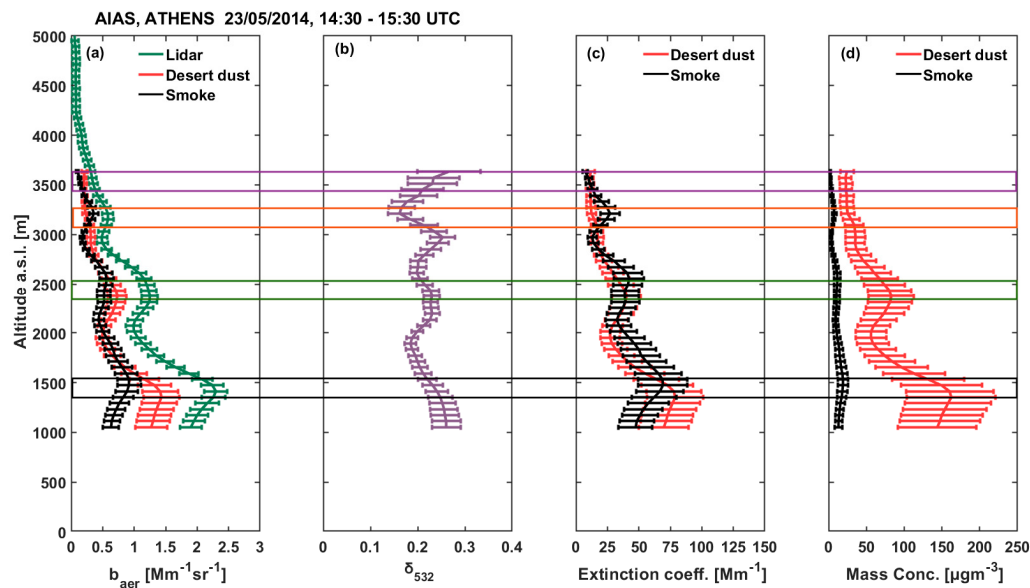


Figure 7. Vertical profiles of the (a) aerosol backscatter coefficient total (lidar-green line), coarse (desert dust-red line) and fine (smoke-black line) modes, (b) particle linear depolarization ratio measured by the AIAS lidar at 532 nm, (c) coarse-mode (desert dust-red line) and fine-mode (smoke-black line) aerosol extinction, and (d) coarse-mode (desert dust-red line) and fine-mode (smoke-black line) aerosol mass concentrations on 23 May 2014.

3.2. Case 26 May 2014: Aged BB and Dust (Unusual Sahara and Kazakhstan Dust Aerosols)

In Figure 8a,b, we present the aerosol optical profiles ($3b + 2a + \delta$) from 26 May, averaged within 19:00–21:45 UTC. Four different layers were identified: layer 1 (1.68–2.04 km), layer 2 (2.28–2.58 km), layer 3 (3.12–3.66 km), and layer 4 (3.90–4.32 km).

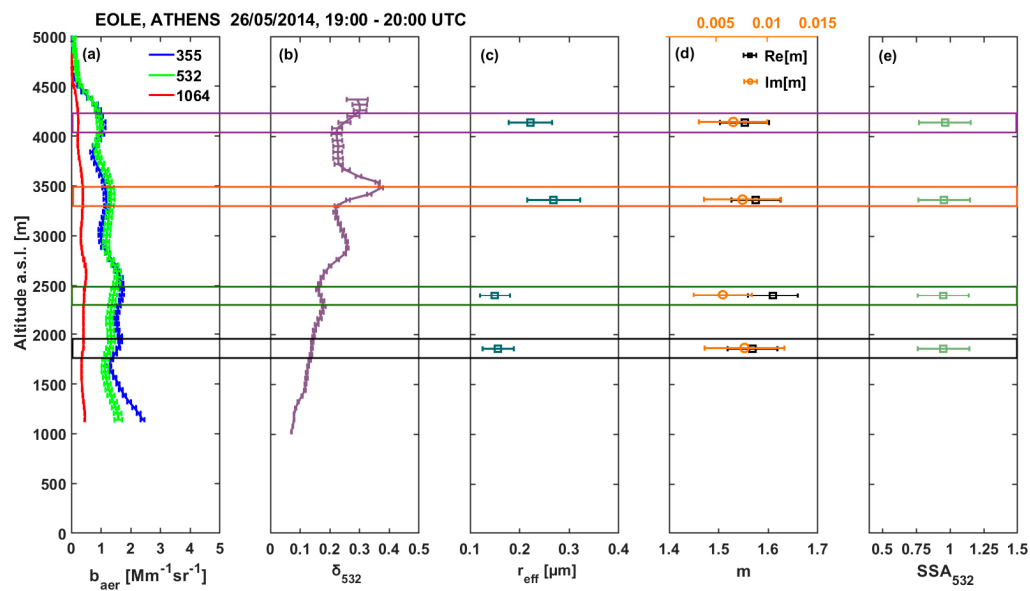


Figure 8. Vertical profiles of the (a) aerosol backscatter at 355 nm (blue line), 532 nm (green line) and 1064 nm (red line) obtained over Athens by the EOLE lidar, (b) particle depolarization ratio (532 nm), (c) the aerosol effective radius, (d) refractive index real part (black line) and imaginary part (orange line), and (e) single-scattering albedo, as estimated by the inversion algorithm using the aerosol optical properties derived from the Raman lidar measurements at 532 nm on 26 May 2014 (19:00–20:00 UTC).

The retrieved aerosol properties (Figure 8a,b) show that the four elevated layers were mostly composed of mixed biomass-burning and dust aerosols, since δ_{532} values were found to take from very low to very high values (7–28%).

The r_{eff} estimations at the first two layers (centered around 1.8 to 2.6 km altitude) showed a significant dominance of fine-mode particles ($r_{\text{eff}} 0.15 \pm 0.03 \mu\text{m}$) (Figure 8c), accompanied by a high number density of $1741 \pm 520 \text{ cm}^{-3}$. However, in the two upper layers (above 3 km), the r_{eff} ranged from 0.22 to 0.27 μm , indicating the predominance of dust particles accompanied by a smaller number density ($455 \pm 137 \text{ cm}^{-3}$), as estimated for both layers.

Furthermore, in Figure 8d, we present the retrieved refractive indices, spanning a range from 1.55 ± 0.05 to 1.61 ± 0.05 for the real part and between 0.006 ± 0.003 to 0.008 ± 0.004 for the imaginary part. Despite the relatively low $\text{Im}[m]$ values, they still highlight the presence of aerosols with absorption capabilities. The SSA mean values were consistently found to be 0.96 ± 0.19 for all four layers (Figure 6e), again indicating the presence of low-absorbing particles, as corroborated by previous findings [20].

In Figure 9, we illustrate four distinct aerosol layers characterized by low-to-moderate backscattering ($0.3\text{--}2.0 \text{ Mm}^{-1} \text{ sr}^{-1}$), reaching an altitude of about 4.5 km a.s.l. (Figure 9a). The first two layers (1.9–2.4 km) exhibited 14–17% depolarization ratios (Figure 9b), typical values associated with a mixture of fine and coarse particles, with the fine mode predominating. The two uppermost layers (3.4–4.1 km) showed higher depolarization ratios (20–28%), indicative of non-spherical dust particles [20,86].

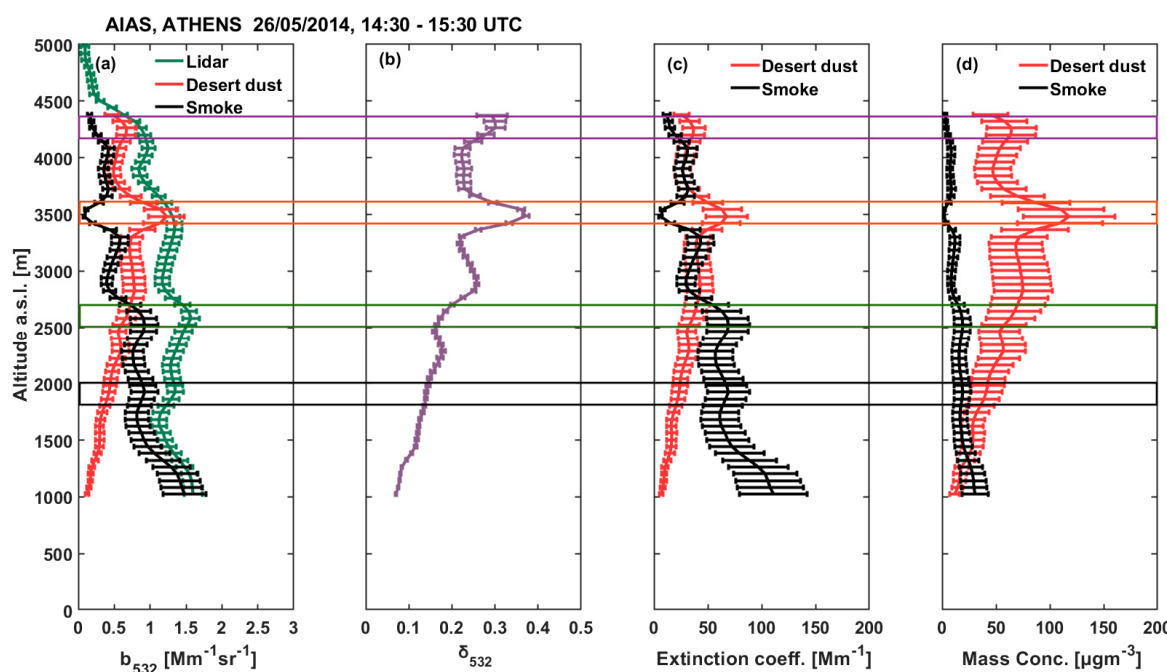


Figure 9. Vertical profiles of the (a) aerosol backscatter coefficient total (lidar-green line), coarse (desert dust-red line) and fine (smoke-black line) modes, (b) particle linear depolarization ratio measured by the AIAS lidar at 532 nm, (c) coarse-mode (desert dust-red line) and fine-mode (smoke-black line) aerosol extinction, and (d) coarse-mode (desert dust-red line) and fine-mode (smoke-black line) aerosol mass concentrations on 26 May 2014.

The fine and coarse mode mean mass specific extinction coefficients were $k_{\text{ext},c} = 0.57 \text{ m}^2 \text{ g}^{-1}$ and $k_{\text{ext},f} = 3.10 \text{ m}^2 \text{ g}^{-1}$, with mean volume concentrations to AOD values equal to $v_c/\text{AOD}_c = 0.67 \times 10^{-6} \text{ m}$ (coarse-mode) and $v_f/\text{AOD}_f = 0.20 \times 10^{-6} \text{ m}$ (fine-mode). As in the previous case of 23 May, lidar ratios of 75 sr and 55 sr were used for the conversion of the aerosol backscatter into the particle extinction coefficients (Figure 9c) for the biomass-burning (fine mode) and desert dust (coarse mode) particles, respectively.

Thus, the dust extinction coefficients were of the order of 30 Mm^{-1} and 50 Mm^{-1} for fine particles.

The elevated dust mass concentrations ranged from 40 ± 16 to $120 \pm 43 \mu\text{g m}^{-3}$ (Figure 9d), with increasing values up to 3.5 km. Regarding the smoke mass concentration, a mean value of about $20 \pm 8 \mu\text{g m}^{-3}$ was estimated, with the maximum $30 \pm 12 \mu\text{g m}^{-3}$ taken below 1.5 km of height. In this case, aged biomass-burning aerosols originating from wildfires in South Russia considerably contributed to the fine mode particle mass. The mean total AOD₅₃₂ derived by the AIAS lidar was found to be 0.25.

3.3. Intercomparison of Aerosol Columnar Retrievals (Lidar and Sun Photometer)

In Figure 10, we discuss the similarity of the aerosol properties derived by the lidar with the ones obtained by CIMEL. Specifically, we present the temporal evolution of the refractive indices Re[m], Im[m], r_{eff}, and SSA (532 and 440 nm), as well as the columnar daily mean AOD (340, 500, 1020 nm) values, using data from both instruments (EOLE lidar and CIMEL sun photometer) for the period of 21–26 May 2014.

More specifically, Figure 10a presents the real part of m obtained by inverting EOLE lidar signals. The values ranged from 1.44 ± 0.05 to 1.61 ± 0.05 and revealed the presence of mixed dust with aged biomass-burning aerosols [83,86,121]. The corresponding values obtained using the sun photometer at various wavelengths (440, 675, 870, and 1020 nm) varied between 1.45 ± 0.07 and 1.50 ± 0.07 and were in accordance with the lidar inversion estimates. The imaginary part (Figure 10b) varied between 0.004 ± 0.002 and 0.008 ± 0.004 , indicating the presence of low-absorbing particles. However, the integrated values of the imaginary part, as obtained by the sun photometer, ranged from 0.0005 to 0.002, an order of magnitude lower compared to the ones derived by the lidar. We should note that the uncertainty of Im[m] depends on its variation due to the wavelength dependence, and its uncertainty increases when non-spherical particles are considered in the retrieval [23]. Thus, in our case, a straightforward evaluation of the vertical variation of Im[m] was not possible due to the significant uncertainty [23].

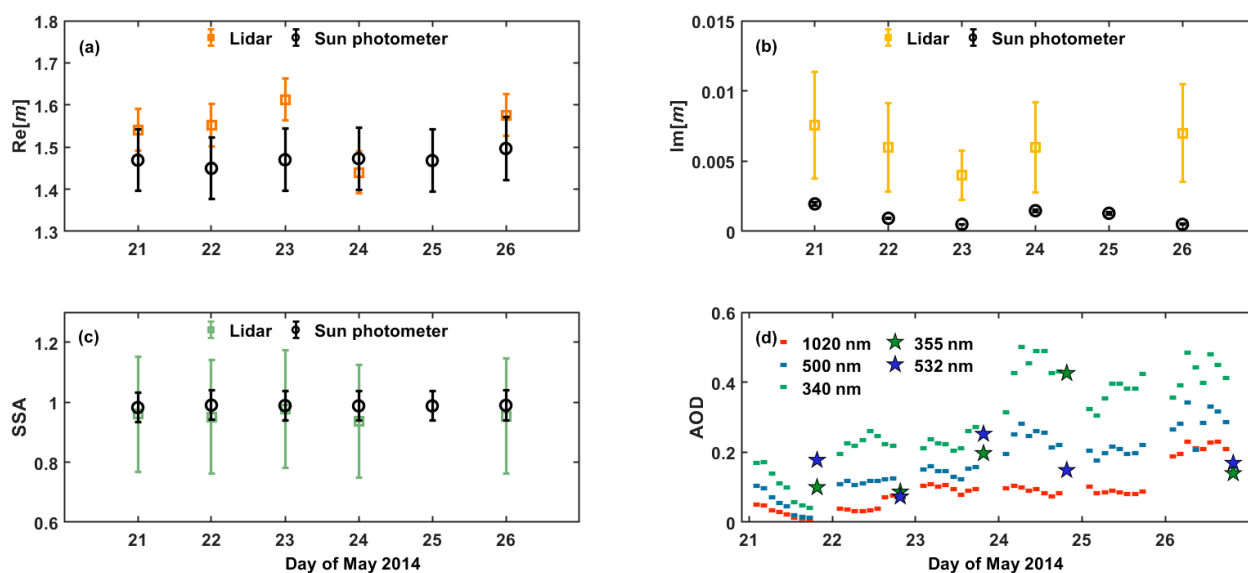


Figure 10. (a) Real part of refractive index Re[m]; (b) imaginary part of refractive index Im[m]; (c) single-scattering albedo (SSA) at 532 nm (green) and 440 nm (black), derived from Raman lidar signal inversions and the CIMEL sun photometer; (d) temporal evolution of the columnar daily mean AOD (340, 500, and 1200 nm), retrieved from CIMEL sun photometer and mean AOD values (355 and 532 nm) and obtained by the EOLE lidar.

The lidar-derived SSA ranged from 0.94 ± 0.19 to 0.97 ± 0.20 (Figure 10c), indicative of a mixture of dust and biomass-burning particles [20,24,86]. The corresponding SSA sun

photometric retrievals (at 440 nm) showed a mean value of about 0.99 ± 0.05 , in a good agreement with the lidar estimations.

In Figure 10d, we present the AOD as obtained using the sun photometer and the Raman lidar. We can observe that the AOD values (from 340 to 1020 nm) increased from about 0.03 to 0.50 (340 nm) and from 0.01 to 0.34 (500 nm), while those derived by the lidar ranged from 0.09–0.43 (355 nm) to 0.07–0.25 (532 nm). Despite the relatively good agreement between the two retrievals, it seems that there were some AOD discrepancies, probably arising from various sources, like (a) measurements that were not temporally synchronous, as -sun photometric data were obtained during daytime and Raman lidar measurements at nighttime; (b) different operation principle between the two instruments—the sun photometer measured the direct solar irradiance in the entire atmospheric column to obtain the AOD, while the layer-derived AOD from lidar was estimated by calculating the integral of the extinction coefficient from heights of ~0.5 to 5.0 km a.s.l. (in our case).

4. Conclusions

This study presents an unusual case of mixed biomass-burning and polluted dust aerosols transported from Kazakhstan and Saharan deserts over Athens, Greece (21 to 26 May 2014). To study this event, we used a synergy of remote sensing instrumentation (multi-wavelength elastic-Raman-depolarization lidar, CIMEL sun photometer) and in situ aerosol sampling, as well as models (microphysical inversion schemes), to retrieve a complete set of the aerosols' optical, microphysical, and chemical properties. The FLEXPART dispersion model analysis highlighted two cases of mixtures: (a) one of biomass-burning and dust aerosols originating predominantly from the South Russia–North and central Kazakhstan and partially from the Saharan desert region (23 May); and (b) one of mixed particles coming from the Saharan desert, with a minor contribution from the southern Russia and northern Kazakhstan areas (26 May). From the lidar observations, we found LR values ranging from 25 to 89 sr (355 nm) and 35 to 70 sr (532 nm), while the δ_{532} values ranged from 7 to 28%. Moreover, the observed $AE_{b355/532}$ and $AE_{b532/1064}$ values were found to be $-0.36\text{--}2.01$ and $0.63\text{--}2.01$, respectively. The significant spread of the observed optical properties indicates the mixing of biomass-burning with mineral dust particles, influenced also by the transport time and the nature of the aerosol sources.

The EBC, EC, and OC concentrations covaried throughout the study, with OC concentrations ranging between $\sim 0.81\text{--}4.44 \mu\text{g m}^{-3}$, influenced by the air mass origin. The analysis of water-soluble ionic species of $PM_{2.5}$ and PM_{10} showed elevated concentrations of NO_3^- , NH_4^+ , SO_4^{2-} , Mg^{2+} , and Ca^{2+} on 21 and 23 May, indicating predominantly anthropogenic and coarse particles.

The columnar mean size distribution retrieved using sun photometric measurements over Athens revealed that, on 21–22 May, the fine smoke particles dominated ($\sim 0.15 \mu\text{m}$), while on 23–26 May, the coarse mode became more pronounced ($\sim 1.7 \mu\text{m}$). The POLIPHON algorithm was used to estimate the vertical profile of the mass concentration for the dust and non-dust components on 23 and 26 May.

Regarding the layer-derived aerosol microphysical properties, we found that the refractive indices ranged from $1.39 (\pm 0.05) + 0.002 (\pm 0.001)i$ to $1.63 (\pm 0.05) + 0.008 (\pm 0.004)i$, with a mean SSA value (532 nm) of approximately 0.96 ± 0.19 , indicating slightly absorbing particles.

A comparison of the retrieved aerosol properties with sun photometric data demonstrated good agreement regarding SSA and $Re[m]$. Although evaluating the variation of $Im[m]$ is challenging due to higher uncertainties, the AOD and AE (440/870) showed very good agreement between the two retrieval methods.

Our study suggests the need for further synergy between in situ aerosol chemical data and multi-wavelength Raman-depolarization lidar measurements to refine the retrieval procedure of unusual mixtures and minimize uncertainties.

Supplementary Materials: The following supporting information can be downloaded at: <https://www.mdpi.com/article/10.3390/atmos15020190/s1>; Figure S1. Mean Sea Level Pressure (white contours in mb) and temperature at 850 mb level (color scale in °C) on 14,15,16,20,21,22 May 2014 from NCEP reanalysis; Figure S2. Mean Sea Level Pressure (white contours in mb) and temperature at 850 mb level (color scale in °C) on 23,24,25,26 May 2014 from NCEP reanalysis; Figure S3. Footprint emission sensitivity for dust obtained by FLEXPART for the air masses arriving over Athens between 1.3 and 1.4 km from 23 to 24 May 2014 (12:00 UTC to 00:00 UTC); Figure S4. Footprint emission sensitivity for dust obtained by FLEXPART for the air masses arriving over Athens between 2.2 and 2.7 km from 23 to 24 May 2014 (12:00 UTC to 00:00 UTC); Figure S5. Footprint emission sensitivity for dust obtained by FLEXPART for the air masses arriving over Athens between 3.1 and 3.5 km from 23 to 24 May 2014 (12:00 UTC to 00:00 UTC); Figure S6. Footprint emission sensitivity for dust obtained by FLEXPART for the air masses arriving over Athens between 3.6 and 3.9 km from 23 to 24 May 2014 (12:00 UTC to 00:00 UTC); Figure S7. Footprint emission sensitivity for dust obtained by FLEXPART for the air masses arriving over Athens between 1.7 and 2.1 km from 26 to 27 May 2014 (12:00 UTC to 00:00 UTC); Figure S8. Footprint emission sensitivity for dust obtained by FLEXPART for the air masses arriving over Athens between 2.3 and 2.6 km from 26 to 27 May 2014 (12:00 UTC to 00:00 UTC); Figure S9. Footprint emission sensitivity for dust obtained by FLEXPART for the air masses arriving over Athens between 3.1 and 3.7 km from 26 to 27 May 2014 (12:00 UTC to 00:00 UTC); Figure S10. Footprint emission sensitivity for dust obtained by FLEXPART for the air masses arriving over Athens between 3.9 and 4.3 km from 26 to 27 May 2014 (12:00 UTC to 00:00 UTC); Figure S11. (a) Geometrical and (b–d) mean optical properties of the aerosol layers observed by the EOLE lidar systems over Athens along with their standard deviation (21–26 May 2014); Figure S12. Temporal variability of mean atmospheric concentrations of PM_{2.5} and PM₁₀ for the sampling period from 21/5/14 to 7/6/14 (A: 11:30–16:30, B: 22:00–01:00); Figure S13. Ratio of PM_{2.5}/PM₁₀ for the sampling period from 21/5/14 to 7/6/14; Figure S14. Temporal variability of daily concentrations of calcium, magnesium, sodium, chloride and potassium in (a) PM_{2.5}, (b) PM₁₀; Figure S15. Temporal variability of daily concentrations of nitrate, sulfate, ammonia and calcium and magnesium ions in (a) PM_{2.5}, (b) PM₁₀; Figure S16. Contribution of ionic species to the mass of (a) PM_{2.5}, (b) PM₁₀; Table S1. Average daily concentration of PM_{2.5} (ng m^{-3}) and ionic fraction (ng m^{-3}) on 23/05/2014; Table S2. Average daily concentration of PM₁₀ (ng m^{-3}) and ionic fraction (ng m^{-3}) on 23/05/2014; Figure S17. Comparison of retrieved particle size distribution for Saharan (SD) and non-Sahara (nSD) cases from Figure 5 (red) and measured (blue) typical Sahara (SD) and background surface aerosol size distributions (aerodynamic diameter) obtained under similar conditions in Athens by means of cascade impactors [102].

Author Contributions: Conceptualization, A.P.; methodology, M.G., A.P. and P.K.; software, M.G., P.K., C.G.Z., N.E., I.V. and S.E.; data analysis, M.G., E.R., S.V., M.I.G. and I.V.; investigation, M.G. and A.P.; writing—original draft preparation, M.G.; writing, M.G., P.K. and A.P.; review and editing, A.P., M.G., P.K., E.R., C.G.Z., M.M., S.V., K.E., M.I.G. and A.A.; visualization, M.G., N.E., S.E., M.I.G. and S.S.; supervision, A.P. All authors have read and agreed to the published version of the manuscript.

Funding: M.G. was supported by the Hellenic Foundation for Research and Innovation (HFRI) under the 4th Call for HFRI Ph.D. Fellowships (Fellowship number: 9293). A.P. and P.K. were supported by the MACAVE research project, implemented within the framework of the action of Supporting of Postdoctoral Researchers of the Operational Program Education and Lifelong Learning (action's beneficiary: General Secretariat for Research and Technology), and were co-financed by the European Social Fund (ESF) and the Greek State. A.P. and A.A. were supported by the EU-ITN-People-MC-ITARS Actions Programme (2012–2016) Grant No. 289923. The FLEXPART results used a virtual access service that is supported by the European Commission under the Horizon 2020—Research and Innovation Framework Programme, H2020-INFRAIA-2020-1, ATMO-ACCESS. Grant Agreement number: 101008004. The computations/simulations/[SIMILAR] were performed using resources provided by Sigma2—the National Infrastructure for High-Performance Computing and Data Storage in Norway. S.E was supported by EYE-CLIMA, a European Union's Horizon Europe research and innovation programme under grant agreement No. 101081395.

Institutional Review Board Statement: Not applicable.

Informed Consent Statement: Not applicable.

Data Availability Statement: The data presented in this study are available on request from the corresponding author. The data are not publicly available as they are part of a larger dataset which is not published yet.

Acknowledgments: We acknowledge V. Amiridis (PI) from the Institute for Space Applications and Remote Sensing and ISARS of the National Observatory of Athens (NOA) for the provision of the NOA AERONET sun photometer data. We acknowledge the use of data and/or imagery from NASA's Fire Information for Resource Management System (FIRMS) (<https://earthdata.nasa.gov/firms>) (accessed on 25 January 2024)), part of NASA's Earth Observing System Data and Information System (EOSDIS). The Biomedical Research Foundation of the Academy of Athens (BRFAA) is acknowledged for the provision of its mobile platform to host the NTUA AIAS lidar system.

Conflicts of Interest: The authors declare no conflicts of interest.

References

1. Creamean, J.M.; Suski, K.J.; Rosenfeld, D.; Cazorla, A.; DeMott, P.J.; Sullivan, R.C.; White, A.B.; Ralph, F.M.; Minnis, P.; Comstock, J.M.; et al. Dust and Biological Aerosols from the Sahara and Asia Influence Precipitation in the Western U.S. *Science* **2013**, *339*, 1572–1578. [[CrossRef](#)]
2. Intergovernmental Panel On Climate Change. *Climate Change 2021—The Physical Science Basis: Working Group I Contribution to the Sixth Assessment Report of the Intergovernmental Panel on Climate Change*, 1st ed.; Cambridge University Press: Cambridge, UK, 2023; ISBN 978-1-00-915789-6.
3. Guo, J.; Lou, M.; Miao, Y.; Wang, Y.; Zeng, Z.; Liu, H.; He, J.; Xu, H.; Wang, F.; Min, M.; et al. Trans-Pacific Transport of Dust Aerosols from East Asia: Insights Gained from Multiple Observations and Modeling. *Environ. Pollut.* **2017**, *230*, 1030–1039. [[CrossRef](#)] [[PubMed](#)]
4. Kok, J.F.; Adebiyi, A.A.; Albani, S.; Balkanski, Y.; Checa-Garcia, R.; Chin, M.; Colarco, P.R.; Hamilton, D.S.; Huang, Y.; Ito, A.; et al. Contribution of the World's Main Dust Source Regions to the Global Cycle of Desert Dust. *Atmos. Chem. Phys.* **2021**, *21*, 8169–8193. [[CrossRef](#)]
5. Caquineau, S.; Gaudichet, A.; Gomes, L.; Legrand, M. Mineralogy of Saharan Dust Transported over Northwestern Tropical Atlantic Ocean in Relation to Source Regions. *J. Geophys. Res. Atmos.* **2002**, *107*, AAC 4-1–AAC 4-12. [[CrossRef](#)]
6. Sokolik, I.; Andronova, A.; Johnson, T.C. Complex Refractive Index of Atmospheric Dust Aerosols. *Atmos. Environ. Part Gen. Top.* **1993**, *27*, 2495–2502. [[CrossRef](#)]
7. Su, L.; Toon, O.B. Saharan and Asian Dust: Similarities and Differences Determined by CALIPSO, AERONET, and a Coupled Climate-Aerosol Microphysical Model. *Atmos. Chem. Phys.* **2011**, *11*, 3263–3280. [[CrossRef](#)]
8. Schuster, G.L.; Vaughan, M.; MacDonnell, D.; Su, W.; Winker, D.; Dubovik, O.; Lapyonok, T.; Trepte, C. Comparison of CALIPSO Aerosol Optical Depth Retrievals to AERONET Measurements, and a Climatology for the Lidar Ratio of Dust. *Atmos. Chem. Phys.* **2012**, *12*, 7431–7452. [[CrossRef](#)]
9. Mamouri, R.E.; Ansmann, A.; Nisantzi, A.; Kokkalis, P.; Schwarz, A.; Hadjimitsis, D. Low Arabian Dust Extinction-to-backscatter Ratio. *Geophys. Res. Lett.* **2013**, *40*, 4762–4766. [[CrossRef](#)]
10. Sokolik, I.; Golitsyn, G. Investigation of Optical and Radiative Properties of Atmospheric Dust Aerosols. *Atmos. Environ. Part Gen. Top.* **1993**, *27*, 2509–2517. [[CrossRef](#)]
11. Golitsyn, G.; Gillette, D.A. Introduction: A Joint Soviet-American Experiment for the Study of Asian Desert Dust and Its Impact on Local Meteorological Conditions and Climate. *Atmos. Environ. Part Gen. Top.* **1993**, *27*, 2467–2470. [[CrossRef](#)]
12. Nazarov, B.I.; Maslov, V.A.; Abdullaev, S.F. Optical and Microphysical Parameters of Arid Dust Aerosol. *Izv. Atmos. Ocean. Phys.* **2010**, *46*, 468–474. [[CrossRef](#)]
13. Nazarov, M.; Noh, D.Y. Rare Earth Double Activated Phosphors for Different Applications. *J. Rare Earths* **2010**, *28*, 1–11. [[CrossRef](#)]
14. Bond, T.C.; Doherty, S.J.; Fahey, D.W.; Forster, P.M.; Berntsen, T.; DeAngelo, B.J.; Flanner, M.G.; Ghan, S.; Kärcher, B.; Koch, D.; et al. Bounding the Role of Black Carbon in the Climate System: A Scientific Assessment. *J. Geophys. Res. Atmos.* **2013**, *118*, 5380–5552. [[CrossRef](#)]
15. Wu, B.; Xuan, K.; Zhang, X.; Shen, X.; Li, X.; Zhou, Q.; Cao, X.; Zhang, H.; Yao, Z. Mass Absorption Cross-Section of Black Carbon from Residential Biofuel Stoves and Diesel Trucks Based on Real-World Measurements. *Sci. Total Environ.* **2021**, *784*, 147225. [[CrossRef](#)]
16. Forster, P.; Ramaswamy, V.; Artaxo, P.; Berntsen, T.; Betts, R.; Fahey, D.W.; Haywood, J.; Lean, J.; Lowe, D.C.; Raga, G.; et al. Changes in Atmospheric Constituents and in Radiative Forcing. In *Climate Change 2007: The Physical Science Basis; Contribution of Working Group I to the Fourth Assessment Report of the Intergovernmental Panel on Climate Change*; Solomon, S., Qin, D., Manning, M., Chen, Z., Marquis, M., Averyt, K.B., Tignor, M., Miller, H.L., Eds.; Cambridge University Press: Cambridge, UK, 2007; pp. 1–106.
17. Carslaw, K.S.; Boucher, O.; Spracklen, D.V.; Mann, G.W.; Rae, J.G.L.; Woodward, S.; Kulmala, M. A Review of Natural Aerosol Interactions and Feedbacks within the Earth System. *Atmos. Chem. Phys.* **2010**, *10*, 1701–1737. [[CrossRef](#)]
18. Jacobson, M.Z. Effects of Biomass Burning on Climate, Accounting for Heat and Moisture Fluxes, Black and Brown Carbon, and Cloud Absorption Effects. *J. Geophys. Res. Atmos.* **2014**, *119*, 8980–9002. [[CrossRef](#)]

19. Liu, L.; Cheng, Y.; Wang, S.; Wei, C.; Pöhlker, M.L.; Pöhlker, C.; Artaxo, P.; Shrivastava, M.; Andreae, M.O.; Pöschl, U.; et al. Impact of Biomass Burning Aerosols on Radiation, Clouds, and Precipitation over the Amazon: Relative Importance of Aerosol–Cloud and Aerosol–Radiation Interactions. *Atmos. Chem. Phys.* **2020**, *20*, 13283–13301. [[CrossRef](#)]
20. Murayama, T.; Müller, D.; Wada, K.; Shimizu, A.; Sekiguchi, M.; Tsukamoto, T. Characterization of Asian Dust and Siberian Smoke with Multi-Wavelength Raman Lidar over Tokyo, Japan in Spring 2003. *Geophys. Res. Lett.* **2004**, *31*, L23103. [[CrossRef](#)]
21. Ansmann, A.; Baars, H.; Tesche, M.; Müller, D.; Althausen, D.; Engelmann, R.; Pauliquevis, T.; Artaxo, P. Dust and Smoke Transport from Africa to South America: Lidar Profiling over Cape Verde and the Amazon Rainforest. *Geophys. Res. Lett.* **2009**, *36*, L11802. [[CrossRef](#)]
22. Sicard, M.; Mallet, M.; Garcia-Vizcaino, D.; Comeón, A.; Rocadenbosch, F.; Dubuisson, P.; Muñoz-Porcar, C. Intense Dust and Extremely Fresh Biomass Burning Outbreak in Barcelona, Spain: Characterization of Their Optical Properties and Estimation of Their Direct Radiative Forcing. *Environ. Res. Lett.* **2012**, *7*, 034016. [[CrossRef](#)]
23. Müller, D.; Veselovskii, I.; Kolgotin, A.; Tesche, M.; Ansmann, A.; Dubovik, O. Vertical Profiles of Pure Dust and Mixed Smoke–Dust Plumes Inferred from Inversion of Multiwavelength Raman/Polarization Lidar Data and Comparison to AERONET Retrievals and in Situ Observations. *Appl. Opt.* **2013**, *52*, 3178. [[CrossRef](#)] [[PubMed](#)]
24. Janicka, L.; Stachlewska, I.S.; Veselovskii, I.; Baars, H. Temporal Variations in Optical and Microphysical Properties of Mineral Dust and Biomass Burning Aerosol Derived from Daytime Raman Lidar Observations over Warsaw, Poland. *Atmos. Environ.* **2017**, *169*, 162–174. [[CrossRef](#)]
25. Bong Park, C.; Sugimoto, N.; Matsui, I.; Shimizu, A.; Tatarov, B.; Kamei, A.; Hie Lee, C.; Uno, I.; Takemura, T.; Westphal, D.L. Long-Range Transport of Saharan Dust to East Asia Observed with Lidars. *SOLA* **2005**, *1*, 121–124. [[CrossRef](#)]
26. Hofer, J.; Althausen, D.; Abdullaev, S.F.; Makhmudov, A.N.; Nazarov, B.I.; Schettler, G.; Engelmann, R.; Baars, H.; Fomba, K.W.; Müller, K.; et al. Long-Term Profiling of Mineral Dust and Pollution Aerosol with Multiwavelength Polarization Raman Lidar at the Central Asian Site of Dushanbe, Tajikistan: Case Studies. *Atmos. Chem. Phys.* **2017**, *17*, 14559–14577. [[CrossRef](#)]
27. Hofer, J.; Ansmann, A.; Althausen, D.; Engelmann, R.; Baars, H.; Abdullaev, S.F.; Makhmudov, A.N. Long-Term Profiling of Aerosol Light Extinction, Particle Mass, Cloud Condensation Nuclei, and Ice-Nucleating Particle Concentration over Dushanbe, Tajikistan, in Central Asia. *Atmos. Chem. Phys.* **2020**, *20*, 4695–4711. [[CrossRef](#)]
28. Müller, D.; Wandinger, U.; Ansmann, A. Microphysical Particle Parameters from Extinction and Backscatter Lidar Data by Inversion with Regularization: Simulation. *Appl. Opt.* **1999**, *38*, 2358. [[CrossRef](#)]
29. Müller, D.; Wandinger, U.; Ansmann, A. Microphysical Particle Parameters from Extinction and Backscatter Lidar Data by Inversion with Regularization: Theory. *Appl. Opt.* **1999**, *38*, 2346. [[CrossRef](#)]
30. Veselovskii, I.; Kolgotin, A.; Griaznov, V.; Müller, D.; Wandinger, U.; Whiteman, D.N. Inversion with Regularization for the Retrieval of Tropospheric Aerosol Parameters from Multiwavelength Lidar Sounding. *Appl. Opt.* **2002**, *41*, 3685. [[CrossRef](#)]
31. Osterloh, L. An Adaptive Base Point Algorithm for the Retrieval of Aerosol Microphysical Properties. *Open Atmos. Sci. J.* **2011**, *5*, 61–73. [[CrossRef](#)]
32. Mamouri, R.E.; Papayannis, A.; Amiridis, V.; Müller, D.; Kokkalis, P.; Rapsomanikis, S.; Karageorgos, E.T.; Tsaknakis, G.; Nenes, A.; Kazadzis, S.; et al. Multi-Wavelength Raman Lidar, Sun Photometric and Aircraft Measurements in Combination with Inversion Models for the Estimation of the Aerosol Optical and Physico-Chemical Properties over Athens, Greece. *Atmos. Meas. Tech.* **2012**, *5*, 1793–1808. [[CrossRef](#)]
33. Papayannis, A.; Mamouri, R.E.; Amiridis, V.; Remoundaki, E.; Tsaknakis, G.; Kokkalis, P.; Veselovskii, I.; Kolgotin, A.; Nenes, A.; Fountoukis, C. Optical-Microphysical Properties of Saharan Dust Aerosols and Composition Relationship Using a Multi-Wavelength Raman Lidar, in Situ Sensors and Modelling: A Case Study Analysis. *Atmos. Chem. Phys.* **2012**, *12*, 4011–4032. [[CrossRef](#)]
34. Labzovskii, L.D.; Papayannis, A.; Binietoglou, I.; Banks, R.F.; Baldasano, J.M.; Toanca, F.; Tzanis, C.G.; Christodoulakis, J. Relative Humidity Vertical Profiling Using Lidar-Based Synergistic Methods in the Framework of the Hygra-CD Campaign. *Ann. Geophys.* **2018**, *36*, 213–229. [[CrossRef](#)]
35. Klett, J.D. Lidar Inversion with Variable Backscatter/Extinction Ratios. *Appl. Opt.* **1985**, *24*, 1638. [[CrossRef](#)] [[PubMed](#)]
36. Bösenberg, J.; Rüdiger, T.; Wulfmeyer, V. *Study on Retrieval Algorithms for a Backscatter Lidar: Final Report*; ESTEC Contract A0/1-2979/95/NL/CN; Max-Planck-Institut Für Meteorologie: Hamburg, Germany, 1997; Volume 226.
37. Renaut, D.; Capitini, R. Boundary-Layer Water Vapor Probing with a Solar-Blind Raman Lidar: Validations, Meteorological Observations and Prospects. *J. Atmos. Ocean. Technol.* **1988**, *5*, 585–601. [[CrossRef](#)]
38. Papayannis, A.; Ancellet, G.; Pelon, J.; Mégie, G. Multiwavelength Lidar for Ozone Measurements in the Troposphere and the Lower Stratosphere. *Appl. Opt.* **1990**, *29*, 467. [[CrossRef](#)]
39. Ansmann, A.; Riebesell, M.; Wandinger, U.; Weitkamp, C.; Voss, E.; Lahmann, W.; Michaelis, W. Combined Raman Elastic-Backscatter LIDAR for Vertical Profiling of Moisture, Aerosol Extinction, Backscatter, and LIDAR Ratio. *Appl. Phys. B Photophysics Laser Chem.* **1992**, *55*, 18–28. [[CrossRef](#)]
40. Mattis, I.; Ansmann, A.; Müller, D.; Wandinger, U.; Althausen, D. Dual-Wavelength Raman Lidar Observations of the Extinction-to-Backscatter Ratio of Saharan Dust. *Geophys. Res. Lett.* **2002**, *29*, 20-1–20-4. [[CrossRef](#)]
41. Freudenthaler, V.; Esselborn, M.; Wiegner, M.; Heese, B.; Tesche, M.; Ansmann, A.; Müller, D.; Althausen, D.; Wirth, M.; Fix, A.; et al. Depolarization Ratio Profiling at Several Wavelengths in Pure Saharan Dust during SAMUM 2006. *Tellus B* **2009**, *61*, 165–179. [[CrossRef](#)]

42. Freudenthaler, V. About the Effects of Polarising Optics on Lidar Signals and the $\Delta 90$ Calibration. *Atmos. Meas. Tech.* **2016**, *9*, 4181–4255. [[CrossRef](#)]
43. Stohl, A.; Hittenberger, M.; Wotawa, G. Validation of the Lagrangian Particle Dispersion Model FLEXPART against Large-Scale Tracer Experiment Data. *Atmos. Environ.* **1998**, *32*, 4245–4264. [[CrossRef](#)]
44. Pisso, I.; Sollum, E.; Grythe, H.; Kristiansen, N.I.; Cassiani, M.; Eckhardt, S.; Arnold, D.; Morton, D.; Thompson, R.L.; Groot Zwaaftink, C.D.; et al. The Lagrangian Particle Dispersion Model FLEXPART Version 10.4. *Geosci. Model Dev.* **2019**, *12*, 4955–4997. [[CrossRef](#)]
45. Hersbach, H.; Bell, B.; Berrisford, P.; Hirahara, S.; Horányi, A.; Muñoz-Sabater, J.; Nicolas, J.; Peubey, C.; Radu, R.; Schepers, D.; et al. The ERA5 Global Reanalysis. *Q. J. R. Meteorol. Soc.* **2020**, *146*, 1999–2049. [[CrossRef](#)]
46. Klimont, Z.; Kupiainen, K.; Heyes, C.; Purohit, P.; Cofala, J.; Rafaj, P.; Borken-Kleefeld, J.; Schöpp, W. Global Anthropogenic Emissions of Particulate Matter Including Black Carbon. *Atmos. Chem. Phys.* **2017**, *17*, 8681–8723. [[CrossRef](#)]
47. Giglio, L.; Randerson, J.T.; van der Werf, G.R. Analysis of Daily, Monthly, and Annual Burned Area Using the Fourth-Generation Global Fire Emissions Database (GFED4). *J. Geophys. Res. Biogeosci.* **2013**, *118*, 317–328. [[CrossRef](#)]
48. Groot Zwaaftink, C.D.; Aas, W.; Eckhardt, S.; Evangelou, N.; Hamer, P.; Johnsrud, M.; Kylling, A.; Platt, S.M.; Stebel, K.; Uggerud, H.; et al. What Caused a Record High PM₁₀ Episode in Northern Europe in October 2020? *Atmos. Chem. Phys.* **2022**, *22*, 3789–3810. [[CrossRef](#)]
49. Giglio, L.; Schroeder, W.; Justice, C.O. The Collection 6 MODIS Active Fire Detection Algorithm and Fire Products. *Remote Sens. Environ.* **2016**, *178*, 31–41. [[CrossRef](#)] [[PubMed](#)]
50. Justice, C.O.; Giglio, L.; Korontzi, S.; Owens, J.; Morisette, J.T.; Roy, D.; Descloitres, J.; Alleaume, S.; Petitcolin, F.; Kaufman, Y. The MODIS Fire Products. *Remote Sens. Environ.* **2002**, *83*, 244–262. [[CrossRef](#)]
51. Giglio, L.; van der Werf, G.R.; Randerson, J.T.; Collatz, G.J.; Kasibhatla, P. Global Estimation of Burned Area Using MODIS Active Fire Observations. *Atmos. Chem. Phys.* **2006**, *6*, 957–974. [[CrossRef](#)]
52. Holben, B.N.; Eck, T.F.; Slutsker, I.; Tanré, D.; Buis, J.P.; Setzer, A.; Vermote, E.; Reagan, J.A.; Kaufman, Y.J.; Nakajima, T.; et al. AERONET—A Federated Instrument Network and Data Archive for Aerosol Characterization. *Remote Sens. Environ.* **1998**, *66*, 1–16. [[CrossRef](#)]
53. Smirnov, A.; Holben, B.N.; Eck, T.F.; Dubovik, O.; Slutsker, I. Cloud-Screening and Quality Control Algorithms for the AERONET Database. *Remote Sens. Environ.* **2000**, *73*, 337–349. [[CrossRef](#)]
54. Eck, T.F.; Holben, B.N.; Giles, D.M.; Slutsker, I.; Sinyuk, A.; Schafer, J.S.; Smirnov, A.; Sorokin, M.; Reid, J.S.; Sayer, A.M.; et al. AERONET Remotely Sensed Measurements and Retrievals of Biomass Burning Aerosol Optical Properties During the 2015 Indonesian Burning Season. *J. Geophys. Res. Atmos.* **2019**, *124*, 4722–4740. [[CrossRef](#)]
55. Dubovik, O.; King, M.D. A Flexible Inversion Algorithm for Retrieval of Aerosol Optical Properties from Sun and Sky Radiance Measurements. *J. Geophys. Res. Atmos.* **2000**, *105*, 20673–20696. [[CrossRef](#)]
56. Dubovik, O.; Sinyuk, A.; Lapyonok, T.; Holben, B.N.; Mishchenko, M.; Yang, P.; Eck, T.F.; Volten, H.; Muñoz, O.; Veihelmann, B.; et al. Application of Spheroid Models to Account for Aerosol Particle Nonsphericity in Remote Sensing of Desert Dust. *J. Geophys. Res. Atmos.* **2006**, *111*, 2005JD006619. [[CrossRef](#)]
57. Panteliadis, P.; Hafkenscheid, T.; Cary, B.; Diapouli, E.; Fischer, A.; Favez, O.; Quincey, P.; Viana, M.; Hitzenberger, R.; Vecchi, R.; et al. ECOC Comparison Exercise with Identical Thermal Protocols after Temperature Offset Correction—Instrument Diagnostics by in-Depth Evaluation of Operational Parameters. *Atmos. Meas. Tech.* **2015**, *8*, 779–792. [[CrossRef](#)]
58. Vratolis, S.; Fetfatzis, P.; Argyrouli, A.; Papayannis, A.; Müller, D.; Veselovskii, I.; Bougiatioti, A.; Nenes, A.; Remoundaki, E.; Diapouli, E.; et al. A New Method to Retrieve the Real Part of the Equivalent Refractive Index of Atmospheric Aerosols. *J. Aerosol Sci.* **2018**, *117*, 54–62. [[CrossRef](#)]
59. Remoundaki, E.; Kassomenos, P.; Mantas, E.; Mihalopoulos, N.; Tsezos, M. Composition and Mass Closure of PM_{2.5} in Urban Environment (Athens, Greece). *Aerosol Air Qual. Res.* **2013**, *13*, 72–82. [[CrossRef](#)]
60. Mantas, E.; Remoundaki, E.; Halari, I.; Kassomenos, P.; Theodosi, C.; Hatzikioseyian, A.; Mihalopoulos, N. Mass Closure and Source Apportionment of PM_{2.5} by Positive Matrix Factorization Analysis in Urban Mediterranean Environment. *Atmos. Environ.* **2014**, *94*, 154–163. [[CrossRef](#)]
61. Veselovskii, I.; Kolgotin, A.; Griaznov, V.; Müller, D.; Franke, K.; Whiteman, D.N. Inversion of Multiwavelength Raman Lidar Data for Retrieval of Bimodal Aerosol Size Distribution. *Appl. Opt.* **2004**, *43*, 1180. [[CrossRef](#)]
62. Tesche, M.; Ansmann, A.; Müller, D.; Althausen, D.; Engelmann, R.; Freudenthaler, V.; Groß, S. Vertically Resolved Separation of Dust and Smoke over Cape Verde Using Multiwavelength Raman and Polarization Lidars during Saharan Mineral Dust Experiment 2008. *J. Geophys. Res. Atmos.* **2009**, *114*, 1–14. [[CrossRef](#)]
63. Ansmann, A.; Seifert, P.; Tesche, M.; Wandinger, U. Profiling of Fine and Coarse Particle Mass: Case Studies of Saharan Dust and Eyjafjallajökull/Grimsvötn Volcanic Plumes. *Atmos. Chem. Phys.* **2012**, *12*, 9399–9415. [[CrossRef](#)]
64. O'Neill, N.T.; Eck, T.F.; Smirnov, A.; Holben, B.N.; Thulasiraman, S. Spectral Discrimination of Coarse and Fine Mode Optical Depth. *J. Geophys. Res. Atmos.* **2003**, *108*, 4559–4573. [[CrossRef](#)]
65. Hess, M.; Koepke, P.; Schult, I. Optical Properties of Aerosols and Clouds: The Software Package OPAC. *Bull. Am. Meteorol. Soc.* **1998**, *79*, 831–844. [[CrossRef](#)]
66. Gasteiger, J.; Groß, S.; Freudenthaler, V.; Wiegner, M. Volcanic Ash from Iceland over Munich: Mass Concentration Retrieved from Ground-Based Remote Sensing Measurements. *Atmos. Chem. Phys.* **2011**, *11*, 2209–2223. [[CrossRef](#)]

67. Mamouri, R.E.; Ansmann, A. Fine and Coarse Dust Separation with Polarization Lidar. *Atmos. Meas. Tech.* **2014**, *7*, 3717–3735. [[CrossRef](#)]
68. Mamouri, R.-E.; Ansmann, A. Potential of Polarization/Raman Lidar to Separate Fine Dust, Coarse Dust, Maritime, and Anthropogenic Aerosol Profiles. *Atmos. Meas. Tech.* **2017**, *10*, 3403–3427. [[CrossRef](#)]
69. Proestakis, E.; Gkikas, A.; Georgiou, T.; Kampouri, A.; Drakaki, E.; Ryder, C.; Marenco, F.; Marinou, E.; Amiridis, V. A Near-Global Multiyear Climate Data Record of the Fine-Mode and Coarse-Mode Components of Atmospheric Pure-Dust. *Atmos. Meas. Tech. Discuss.* **2024**, *2024*, 1–56.
70. Reid, J.S.; Eck, T.F.; Christopher, S.A.; Koppmann, R.; Dubovik, O.; Eleuterio, D.P.; Holben, B.N.; Reid, E.A.; Zhang, J. A Review of Biomass Burning Emissions Part III: Intensive Optical Properties of Biomass Burning Particles. *Atmos. Chem. Phys.* **2005**, *5*, 827–849. [[CrossRef](#)]
71. Cozic, J.; Mertes, S.; Verheggen, B.; Cziczo, D.J.; Gallavardin, S.J.; Walter, S.; Baltensperger, U.; Weingartner, E. Black Carbon Enrichment in Atmospheric Ice Particle Residuals Observed in Lower Tropospheric Mixed Phase Clouds. *J. Geophys. Res. Atmos.* **2008**, *113*. [[CrossRef](#)]
72. Bukowiecki, N.; Zieger, P.; Weingartner, E.; Jurányi, Z.; Gysel, M.; Neininger, B.; Schneider, B.; Hueglin, C.; Ulrich, A.; Wichser, A.; et al. Ground-Based and Airborne in-Situ Measurements of the Eyjafjallajökull Volcanic Aerosol Plume in Switzerland in Spring 2010. *Atmos. Chem. Phys.* **2011**, *11*, 10011–10030. [[CrossRef](#)]
73. Engelhart, G.J.; Hennigan, C.J.; Miracolo, M.A.; Robinson, A.L.; Pandis, S.N. Cloud Condensation Nuclei Activity of Fresh Primary and Aged Biomass Burning Aerosol. *Atmos. Chem. Phys.* **2012**, *12*, 7285–7293. [[CrossRef](#)]
74. Tesche, M.; Müller, D.; Gross, S.; Ansmann, A.; Althausen, D.; Freudenthaler, V.; Weinzierl, B.; Veira, A.; Petzold, A. Optical and Microphysical Properties of Smoke over Cape Verde Inferred from Multiwavelength Lidar Measurements. *Tellus B Chem. Phys. Meteorol.* **2011**, *63*, 677. [[CrossRef](#)]
75. Wang, T.; Han, Y.; Hua, W.; Tang, J.; Huang, J.; Zhou, T.; Huang, Z.; Bi, J.; Xie, H. Profiling Dust Mass Concentration in Northwest China Using a Joint Lidar and Sun-Photometer Setting. *Remote Sens.* **2021**, *13*, 1099. [[CrossRef](#)]
76. Ansmann, A.; Tesche, M.; Seifert, P.; Groß, S.; Freudenthaler, V.; Apituley, A.; Wilson, K.M.; Serikov, I.; Linné, H.; Heinold, B.; et al. Ash and Fine-Mode Particle Mass Profiles from EARLINET-AERONET Observations over Central Europe after the Eruptions of the Eyjafjallajökull Volcano in 2010. *J. Geophys. Res. Atmos.* **2011**, *116*. [[CrossRef](#)]
77. Ansmann, A.; Ohneiser, K.; Mamouri, R.-E.; Knopf, D.A.; Veselovskii, I.; Baars, H.; Engelmann, R.; Foth, A.; Jimenez, C.; Seifert, P.; et al. Tropospheric and Stratospheric Wildfire Smoke Profiling with Lidar: Mass, Surface Area, CCN, and INP Retrieval. *Atmos. Chem. Phys.* **2021**, *21*, 9779–9807. [[CrossRef](#)]
78. Ansmann, A.; Mamouri, R.-E.; Hofer, J.; Baars, H.; Althausen, D.; Abdullaev, S.F. Dust Mass, Cloud Condensation Nuclei, and Ice-Nucleating Particle Profiling with Polarization Lidar: Updated POLIPHON Conversion Factors from Global AERONET Analysis. *Atmos. Meas. Tech.* **2019**, *12*, 4849–4865. [[CrossRef](#)]
79. Rudich, Y.; Khersonsky, O.; Rosenfeld, D. Treating Clouds with a Grain of Salt. *Geophys. Res. Lett.* **2002**, *29*, 17-1–17-4. [[CrossRef](#)]
80. Micklin, P. The Aral Sea Disaster. *Annu. Rev. Earth Planet. Sci.* **2007**, *35*, 47–72. [[CrossRef](#)]
81. Micklin, P. The Past, Present, and Future Aral Sea. *Lakes Reserv. Sci. Policy Manag. Sustain. Use* **2010**, *15*, 193–213. [[CrossRef](#)]
82. Ginoux, P.; Prospero, J.M.; Gill, T.E.; Hsu, N.C.; Zhao, M. Global-Scale Attribution of Anthropogenic and Natural Dust Sources and Their Emission Rates Based on MODIS Deep Blue Aerosol Products. *Rev. Geophys.* **2012**, *50*. [[CrossRef](#)]
83. Nicolae, D.; Nemuc, A.; Müller, D.; Talianu, C.; Vasilescu, J.; Belegante, L.; Kolgotin, A. Characterization of Fresh and Aged Biomass Burning Events Using Multiwavelength Raman Lidar and Mass Spectrometry. *J. Geophys. Res. Atmos.* **2013**, *118*, 2956–2965. [[CrossRef](#)]
84. Groß, S.; Esselborn, M.; Weinzierl, B.; Wirth, M.; Fix, A.; Petzold, A. Aerosol Classification by Airborne High Spectral Resolution Lidar Observations. *Atmos. Chem. Phys.* **2013**, *13*, 2487–2505. [[CrossRef](#)]
85. Papagiannopoulos, N.; Mona, L.; Amodeo, A.; D’Amico, G.; Gumà Claramunt, P.; Pappalardo, G.; Alados-Arboledas, L.; Guerrero-Rascado, J.L.; Amiridis, V.; Kokkalis, P.; et al. An Automatic Observation-Based Aerosol Typing Method for EARLINET. *Atmos. Chem. Phys.* **2018**, *18*, 15879–15901. [[CrossRef](#)]
86. Soupiona, O.; Papayannis, A.; Kokkalis, P.; Foskinis, R.; Sánchez Hernández, G.; Ortiz-Amezcu, P.; Mylonaki, M.; Papanikolaou, C.-A.; Papagiannopoulos, N.; Samaras, S.; et al. EARLINET Observations of Saharan Dust Intrusions over the Northern Mediterranean Region (2014–2017): Properties and Impact on Radiative Forcing. *Atmos. Chem. Phys.* **2020**, *20*, 15147–15166. [[CrossRef](#)]
87. Mylonaki, M.; Papayannis, A.; Anagnou, D.; Veselovskii, I.; Papanikolaou, C.-A.; Kokkalis, P.; Soupiona, O.; Foskinis, R.; Gidarakou, M.; Kralli, E. Optical and Microphysical Properties of Aged Biomass Burning Aerosols and Mixtures, Based on 9-Year Multiwavelength Raman Lidar Observations in Athens, Greece. *Remote Sens.* **2021**, *13*, 3877. [[CrossRef](#)]
88. Veselovskii, I.; Hu, Q.; Goloub, P.; Podvin, T.; Korenskiy, M.; Derimian, Y.; Legrand, M.; Castellanos, P. Variability in Lidar-Derived Particle Properties over West Africa Due to Changes in Absorption: Towards an Understanding. *Atmos. Chem. Phys.* **2020**, *20*, 6563–6581. [[CrossRef](#)]
89. Theodosi, C.; Grivas, G.; Zarmpas, P.; Chaloulakou, A.; Mihalopoulos, N. Mass and Chemical Composition of Size-Segregated Aerosols (PM_1 , $\text{PM}_{2.5}$, PM_{10}) over Athens, Greece: Local versus Regional Sources. *Atmos. Chem. Phys.* **2011**, *11*, 11895–11911. [[CrossRef](#)]

90. Triantafyllou, E.; Diapouli, E.; Tsilibari, E.M.; Adamopoulos, A.D.; Biskos, G.; Eleftheriadis, K. Assessment of Factors Influencing PM Mass Concentration Measured by Gravimetric & Beta Attenuation Techniques at a Suburban Site. *Atmos. Environ.* **2016**, *131*, 409–417. [[CrossRef](#)]
91. Zhou, Y.; Zheng, N.; Luo, L.; Zhao, J.; Qu, L.; Guan, H.; Xiao, H.; Zhang, Z.; Tian, J.; Xiao, H. Biomass Burning Related Ammonia Emissions Promoted a Self-Amplifying Loop in the Urban Environment in Kunming (SW China). *Atmos. Environ.* **2021**, *253*, 118138. [[CrossRef](#)]
92. Violaki, K.; Tsiodra, I.; Nenes, A.; Tsagkaraki, M.; Kouvarakis, G.; Zarmpas, P.; Florou, K.; Panagiotopoulos, C.; Ingall, E.; Weber, R.; et al. Water Soluble Reactive Phosphate (SRP) in Atmospheric Particles over East Mediterranean: The Importance of Dust and Biomass Burning Events. *Sci. Total Environ.* **2022**, *830*, 154263. [[CrossRef](#)]
93. Ambade, B. Characterization of PM₁₀ over Urban and Rural Sites of Rajnandgaon, Central India. *Nat. Hazards* **2016**, *80*, 589–604. [[CrossRef](#)]
94. Gautam, A.S.; Kumar, S.; Gautam, S.; Singh, K.; Ram, K.; Siingh, D.; Ambade, B.; Sharma, M. Regional Air Quality: Biomass Burning Impacts of SO₂ Emissions on Air Quality in the Himalayan Region of Uttarakhand, India. *Air Qual. Atmos. Health* **2023**, *17*, 1–18. [[CrossRef](#)]
95. Remoundaki, E.; Papayannis, A.; Kassomenos, P.; Mantas, E.; Kokkalis, P.; Tsezos, M. Influence of Saharan Dust Transport Events on PM_{2.5} Concentrations and Composition over Athens. *Water. Air. Soil Pollut.* **2013**, *224*, 1373. [[CrossRef](#)]
96. Wang, C.-F.; Chang, C.-Y.; Tsai, S.-F.; Chiang, H.-L. Characteristics of Road Dust from Different Sampling Sites in Northern Taiwan. *J. Air Waste Manag. Assoc.* **2005**, *55*, 1236–1244. [[CrossRef](#)]
97. Duvall, R.M.; Majestic, B.J.; Shafer, M.M.; Chuang, P.Y.; Simoneit, B.R.T.; Schauer, J.J. The Water-Soluble Fraction of Carbon, Sulfur, and Crustal Elements in Asian Aerosols and Asian Soils. *Atmos. Environ.* **2008**, *42*, 5872–5884. [[CrossRef](#)]
98. Zhang, X.; Hecobian, A.; Zheng, M.; Frank, N.H.; Weber, R.J. Biomass Burning Impact on PM_{2.5} over the Southeastern US during 2007: Integrating Chemically Speciated FRM Filter Measurements, MODIS Fire Counts and PMF Analysis. *Atmos. Chem. Phys.* **2010**, *10*, 6839–6853. [[CrossRef](#)]
99. Miller, R.M.; McFarquhar, G.M.; Rauber, R.M.; O'Brien, J.R.; Gupta, S.; Segal-Rozenhaimer, M.; Dobracki, A.N.; Sedlacek, A.J.; Burton, S.P.; Howell, S.G.; et al. Observations of Supermicron-Sized Aerosols Originating from Biomass Burning in Southern Central Africa. *Atmos. Chem. Phys.* **2021**, *21*, 14815–14831. [[CrossRef](#)]
100. Kaskaoutis, D.G.; Dumka, U.C.; Rashki, A.; Psiloglou, B.E.; Gavril, A.; Mofidi, A.; Petrinoli, K.; Karagiannis, D.; Kambezidis, H.D. Analysis of Intense Dust Storms over the Eastern Mediterranean in March 2018: Impact on Radiative Forcing and Athens Air Quality. *Atmos. Environ.* **2019**, *209*, 23–39. [[CrossRef](#)]
101. Lee, J.; Kim, J.; Song, C.H.; Kim, S.B.; Chun, Y.; Sohn, B.J.; Holben, B.N. Characteristics of Aerosol Types from AERONET Sunphotometer Measurements. *Atmos. Environ.* **2010**, *44*, 3110–3117. [[CrossRef](#)]
102. Gini, M.; Manousakas, M.; Karydas, A.G.; Eleftheriadis, K. Mass Size Distributions, Composition and Dose Estimates of Particulate Matter in Saharan Dust Outbreaks. *Environ. Pollut.* **2022**, *298*, 118768. [[CrossRef](#)] [[PubMed](#)]
103. Eleftheriadis, K.; Ochsenkuhn, K.M.; Lymeropoulou, T.; Karanasiou, A.; Razos, P.; Ochsenkuhn-Petropoulou, M. Influence of Local and Regional Sources on the Observed Spatial and Temporal Variability of Size Resolved Atmospheric Aerosol Mass Concentrations and Water-Soluble Species in the Athens Metropolitan Area. *Atmos. Environ.* **2014**, *97*, 252–261. [[CrossRef](#)]
104. Osborne, S.R.; Johnson, B.T.; Haywood, J.M.; Baran, A.J.; Harrison, M.A.J.; McConnell, C.L. Physical and Optical Properties of Mineral Dust Aerosol during the Dust and Biomass-Burning Experiment. *J. Geophys. Res. Atmos.* **2008**, *113*. [[CrossRef](#)]
105. Weinzierl, B.; Petzold, A.; Esselborn, M.; Wirth, M.; Rasp, K.; Kandler, K.; Schütz, L.; Koepke, P.; Fiebig, M. Airborne Measurements of Dust Layer Properties, Particle Size Distribution and Mixing State of Saharan Dust during SAMUM 2006. *Tellus B* **2009**, *61*, 96–117. [[CrossRef](#)]
106. Sicard, M.; Guerrero-Rascado, J.L.; Navas-Guzmán, F.; Preißler, J.; Molero, F.; Tomás, S.; Bravo-Aranda, J.A.; Comerón, A.; Rocadenbosch, F.; Wagner, F.; et al. Monitoring of the Eyjafjallajökull Volcanic Aerosol Plume over the Iberian Peninsula by Means of Four EARLINET Lidar Stations. *Atmos. Chem. Phys.* **2012**, *12*, 3115–3130. [[CrossRef](#)]
107. Burton, S.P.; Ferrare, R.A.; Hostetler, C.A.; Hair, J.W.; Rogers, R.R.; Oblad, M.D.; Butler, C.F.; Cook, A.L.; Harper, D.B.; Froyd, K.D. Aerosol Classification Using Airborne High Spectral Resolution Lidar Measurements—Methodology and Examples. *Atmos. Meas. Tech.* **2012**, *5*, 73–98. [[CrossRef](#)]
108. Menut, L.; Flamant, C.; Pelon, J.; Flamant, P.H. Urban Boundary-Layer Height Determination from Lidar Measurements over the Paris Area. *Appl. Opt.* **1999**, *38*, 945. [[CrossRef](#)]
109. Ebert, M.; Weinbruch, S.; Rausch, A.; Gorzawski, G.; Helas, G.; Hoffmann, P.; Wex, H. Complex Refractive Index of Aerosols during LACE 98#x2019; as Derived from the Analysis of Individual Particles. *J. Geophys. Res. Atmos.* **2002**, *107*, LAC 3-1–LAC 3-15. [[CrossRef](#)]
110. Petzold, A.; Rasp, K.; Weinzierl, B.; Esselborn, M.; Hamburger, T.; Dörnbrac, A.; Kandler, K.; Schütz, L.; Knippertz, P.; Fiebig, M.; et al. Saharan Dust Absorption and Refractive Index from Aircraft-Based Observations during SAMUM 2006. *Tellus B Chem. Phys. Meteorol.* **2009**, *61*, 118. [[CrossRef](#)]
111. Patterson, E.M.; Gillette, D.A.; Stockton, B.H. Complex Index of Refraction between 300 and 700 Nm for Saharan Aerosols. *J. Geophys. Res.* **1977**, *82*, 3153–3160. [[CrossRef](#)]
112. Sokolik, I.N.; Toon, O.B. Incorporation of Mineralogical Composition into Models of the Radiative Properties of Mineral Aerosol from UV to IR Wavelengths. *J. Geophys. Res. Atmos.* **1999**, *104*, 9423–9444. [[CrossRef](#)]

113. Ebert, M.; Weinbruch, S.; Hoffmann, P.; Ortner, H.M. The Chemical Composition and Complex Refractive Index of Rural and Urban Influenced Aerosols Determined by Individual Particle Analysis. *Atmos. Environ.* **2004**, *38*, 6531–6545. [[CrossRef](#)]
114. Kandler, K.; Schütz, L.; Deutscher, C.; Ebert, M.; Hofmann, H.; Jäckel, S.; Jaenicke, R.; Knippertz, P.; Lieke, K.; Massling, A.; et al. Size Distribution, Mass Concentration, Chemical and Mineralogical Composition and Derived Optical Parameters of the Boundary Layer Aerosol at Tinfou, Morocco, during SAMUM 2006. *Tellus B Chem. Phys. Meteorol.* **2009**, *61*, 32. [[CrossRef](#)]
115. Diapouli, E.; Popovicheva, O.; Kistler, M.; Vratolis, S.; Persiantseva, N.; Timofeev, M.; Kasper-Giebl, A.; Eleftheriadis, K. Physicochemical Characterization of Aged Biomass Burning Aerosol after Long-Range Transport to Greece from Large Scale Wildfires in Russia and Surrounding Regions, Summer 2010. *Atmos. Environ.* **2014**, *96*, 393–404. [[CrossRef](#)]
116. Müller, D.; Ansmann, A.; Mattis, I.; Tesche, M.; Wandinger, U.; Althausen, D.; Pisani, G. Aerosol-Type-Dependent Lidar Ratios Observed with Raman Lidar. *J. Geophys. Res. Atmos.* **2007**, *112*. [[CrossRef](#)]
117. Granados-Muñoz, M.J.; Navas-Guzmán, F.; Guerrero-Rascado, J.L.; Bravo-Aranda, J.A.; Binietoglou, I.; Pereira, S.N.; Basart, S.; Baldasano, J.M.; Belegante, L.; Chaikovsky, A.; et al. Profiling of Aerosol Microphysical Properties at Several EARLINET/AERONET Sites during the July 2012 ChArMEx/EMEP Campaign. *Atmos. Chem. Phys.* **2016**, *16*, 7043–7066. [[CrossRef](#)]
118. Wandinger, U.; Baars, H.; Engelmann, R.; Hünerbein, A.; Horn, S.; Kanitz, T.; Donovan, D.; Van Zadelhoff, G.-J.; Daou, D.; Fischer, J.; et al. HETEAC: The Aerosol Classification Model for EarthCARE. *EPJ Web Conf.* **2016**, *119*, 01004. [[CrossRef](#)]
119. Soupiona, O.; Samaras, S.; Ortiz-Amezcua, P.; Böckmann, C.; Papayannis, A.; Moreira, G.A.; Benavent-Oltra, J.A.; Guerrero-Rascado, J.L.; Bedoya-Velásquez, A.E.; Olmo, F.J.; et al. Retrieval of Optical and Microphysical Properties of Transported Saharan Dust over Athens and Granada Based on Multi-Wavelength Raman Lidar Measurements: Study of the Mixing Processes. *Atmos. Environ.* **2019**, *214*, 116824. [[CrossRef](#)]
120. Alados-Arboledas, L.; Müller, D.; Guerrero-Rascado, J.L.; Navas-Guzmán, F.; Pérez-Ramírez, D.; Olmo, F.J. Optical and Microphysical Properties of Fresh Biomass Burning Aerosol Retrieved by Raman Lidar, and Star-and Sun-Photometry. *Geophys. Res. Lett.* **2011**, *38*. [[CrossRef](#)]
121. Müller, D.; Mattis, I.; Wandinger, U.; Ansmann, A.; Althausen, D.; Stohl, A. Raman Lidar Observations of Aged Siberian and Canadian Forest Fire Smoke in the Free Troposphere over Germany in 2003: Microphysical Particle Characterization. *J. Geophys. Res. Atmos.* **2005**, *110*, 2004JD005756. [[CrossRef](#)]

Disclaimer/Publisher’s Note: The statements, opinions and data contained in all publications are solely those of the individual author(s) and contributor(s) and not of MDPI and/or the editor(s). MDPI and/or the editor(s) disclaim responsibility for any injury to people or property resulting from any ideas, methods, instructions or products referred to in the content.